

UCRL- 98571
PREPRINT



STELLAR

TIME-DEPENDENT MODELS OF RADIATIVELY DRIVEN
STELLAR WINDS: II. NONLINEAR EVOLUTION
OF INSTABILITIES FOR A PURE-ABSORPTION MODEL

Stanley P. Owocki
John I. Castor

Astrophysical Journal

1988

Lawrence
Livermore
National
Laboratory

This is a preprint of a paper intended for publication in a journal or proceedings. Since changes may be made before publication, this preprint is made available with the understanding that it will not be cited or reproduced without the permission of the author.

DISCLAIMER

This document was prepared as an account of work sponsored by an agency of the United States Government. Neither the United States Government nor the University of California nor any of their employees, makes any warranty, express or implied, or assumes any legal liability or responsibility for the accuracy, completeness, or usefulness of any information, apparatus, product, or process disclosed, or represents that its use would not infringe privately owned rights. Reference herein to any specific commercial products, process, or service by trade name, trademark, manufacturer, or otherwise, does not necessarily constitute or imply its endorsement recommendation, or favoring of the United States Government or the University of California. The views and opinions of authors expressed herein do not necessarily state or reflect those of the United States Government or the University of California, and shall not be used for advertising or product endorsement purposes.

**Time-Dependent Models of Radiatively Driven Stellar Winds:
II. Nonlinear Evolution of Instabilities for a Pure-Absorption Model**

Stanley P. Owocki, Bartol Research Institute of the University of Delaware
John I. Castor, Lawrence Livermore National Laboratory
and
George B. Rybicki, Harvard-Smithsonian Center for Astrophysics

Received: _____

ABSTRACT

We describe results of numerical radiation-hydrodynamics simulations of the nonlinear evolution of instabilities in radiatively driven stellar winds. For computational tractability, the wind is idealized as a spherically symmetric, isothermal flow driven by pure absorption of stellar radiation in a fixed ensemble of spectral lines. The simulations indicate that, because of the sensitive velocity dependence of the line-force, there is a strong tendency for the unstable flow to form rather sharp rarefactions in which the highest speed material has very low density. Accordingly line-shadowing effects that played a prominent role in previous models are of greatly reduced importance here. The growth of wave perturbations thus remains nearly exponential well beyond the linear regime, until the waves are kinematically steepened into strong shocks. Unlike in previous models, where *forward* shocks were assumed to abruptly *accelerate* ambient wind material as it is rammed by a dense, strongly driven flow, the strongest shocks here are *reverse* shocks that arise to *decelerate* high-speed, rarefied flow as it impacts slower material that has been compressed into dense shells. The subsequent wind evolution shows a slow decay of the shocks and the gradual thermal decompression and interaction of the dense shells. Since the wind properties have been simplified and rescaled, the results are not quantitatively applicable to actual stars. Nonetheless, their qualitative features agree well with the requirements of displaced narrow absorption components in UV lines, and possibly also of observations of soft X-rays, enhanced infrared flux, and non-thermal radio emission. In addition, gross wind properties like the terminal flow speed and the time-averaged mass loss rate appear in good agreement with values inferred from previous steady wind models, despite the presence of extensive wind structure.

I. INTRODUCTION

The brightest, hottest, most massive stars, the ones referred to as types O, B, and WR, have been revealed by rocket and satellite ultraviolet spectroscopy (Morton 1967; Lamers and Morton 1976) to be the sources of very strong stellar winds. These winds are thought to be driven by the line absorption of the star's continuum radiative momentum flux (Lucy and Solomon 1970; Castor, Abbott, and Klein 1975, hereafter CAK); indeed, theoretical models (Abbott 1980, 1982) based on this line-driving mechanism yield predictions of such mean wind properties as the total mass loss rate and terminal flow speed that are in good agreement with values inferred from observation (Abbott 1978, 1982; Cassinelli 1979). However, such smooth, steady wind models seem inherently incapable of explaining several other observational characteristics of these stars that indicate a high degree of wind structure and variability. Furthermore, linear stability analyses (MacGregor, Hartmann, and Raymond 1979; Martens 1979; Carlberg 1980; Owocki and Rybicki 1984, 1985, 1986) have now demonstrated quite convincingly that such a line-driven wind should be extremely unstable, and it is widely supposed that the nonlinear growth of this instability is responsible for the wind structure. Nonetheless, until recently no method for dynamically calculating the nonlinear evolution of initially small amplitude perturbations has been available, and this has severely limited our ability to build a clear physical picture of the wind structure. This series of papers is devoted to development and application of numerical radiation-hydrodynamics methods for systematically studying the nonlinear evolution of this instability. This paper reports on initial results from applying the code described in Castor, Owocki, and Rybicki (1988, hereafter Paper I) to a simulation of the nonlinear evolution of instabilities in a simplified model in which the wind is driven by pure-absorption lines.

The empirical evidence for extensive structure in hot-star winds includes observations made in the radio, infrared, X-ray, and ultraviolet. Radio observations of these stars made with the VLA often show a distinctly nonthermal emission (Abbott, Bieging, and Churchwell 1981, 1984) thought to originate from synchrotron radiation by particles accelerated in shocks (White 1985). The observed infrared emission is often larger than expected from a smooth wind with the mass loss rate inferred from radio or UV (Abbott et al. 1984), perhaps reflecting a clumpiness that increases the mean square density, and hence the emission measure, of the regions of infrared emission. In soft X-rays, these stars were found with the *Einstein Observatory* to be surprisingly strong sources (Hamnden et al. 1979; Seward et al. 1979), and the detailed character of this X-ray emission supports the idea that it originates from shock-heated gas in the wind. The X-ray luminosity is observed to scale with the bolometric luminosity as $L_x \approx 10^{-7} L_{bol}$, suggesting that the X-ray producing mechanism, like the wind, is directly coupled to the star's radiative energy output. Furthermore, the observed proportion of soft X-rays (Cassinelli and Swank 1983) is greater than would result if the X-ray emission were confined to a narrow corona at the base of the wind (Cassinelli and Olson 1979), suggesting that they are instead emitted in an extended region, such as from shocks spread throughout the wind. (However, subsequent calculations by Waldron [1984] that include the effect of X-ray photoionization indicate that the base corona model may still be viable.)

The ultraviolet spectral line observations of hot stars likewise have several characteristics that seem to point to the existence of extensive structure within the wind itself. First, some of the strongest observed lines are from ions with ionization stages (e.g., CIV, NV, OVI) much higher than characteristic of the stellar temperature (Rogerson and Lamers 1975); these are believed to be produced *via* the Auger ionization process by the above-mentioned soft X-rays (Cassinelli 1979). Secondly, the blue-shifted absorption cores of strong resonance lines are nearly "black", with almost none of the forward-scattered residual emission predicted by steady wind models; this is thought to result from the net backscattering that arises when line photons

resonantly scatter in a highly non-monotonic velocity field, such as in a wind with numerous strong shocks (Lucy 1982a). Finally, superposed upon the broad P-Cygni profiles of strong, but unsaturated lines there often appear variable "narrow absorption components" (Lamers, Gathier, and Snow 1982; Henrichs 1984; Prinja and Howarth 1986, 1988); these are likely to be a direct manifestation of dense clumps propagating through the wind. The persistence of similar narrow components in observations separated by several months has been seen as problematical, since this is much longer than a characteristic wind flow time, which is less than a day. However, more recent high-time-resolution *IUE* observations show that components do vary over a few hours, and recur about every day (Prinja, Howarth, and Henrichs 1987; Prinja and Howarth 1988). Often they first appear as broad absorption enhancements at relatively low velocities ($\approx 0.5V_\infty$) that then gradually narrow and shift to higher velocities ($\approx 0.8V_\infty$), as might be expected from dense clumps that are accelerated outward with the wind.

There are several alternative semi-empirical models for this inferred wind structure, including, for example, episodic mass ejection from the stellar surface (Henrichs 1984; Henrichs et al. 1983), or co-rotating interaction regions between fast and slow wind streams (Mullan 1984a,b, 1986). A more widely held view is that much or all of this observationally inferred structure may be the consequence of the known strong instability of the line-driven flow. Small scale increases in the wind flow speed shift the local line absorption, by the Doppler effect, out of the shadow of intervening material, leading to an increased radiation force that further increases the flow speed. Detailed stability analyses (Owocki and Rybicki 1984; 1985) show that in the supersonic portion of the wind, perturbations with a scale length small compared with a Sobolev length (over which the background flow speed increases by an ion thermal speed) have an initial linear growth rate 50-100 times a typical wind expansion rate. This implies that even very small-amplitude fluctuations at the wind base will quickly grow to nonlinear amplitude as they propagate outward into the wind, perhaps leading to shocks and dense shells that give rise to the observational signatures.

Until now no calculation of the nonlinear evolution of perturbations has been available, and so previous models have simply assumed, or guessed, that the instability will lead to a specific form of wind structure that includes shocks. For example, in Lucy's (1982b) periodic-shock model, this assumed flow structure consists of a periodic train of shocks whose strength and separation are controlled by the competition between the line-driven flow instability and the effect of shadowing by shocks closer to the star; given this scenario, one can work out approximate solutions to the flow equations and even derive predictions for observational signatures such as the luminosity and spectrum of X-ray emission. Another example is the Krölik and Raymond (1985) episodic-shell model, in which the flow structure is assumed to consist of a single, isolated shell bounded by a shock; this model treats in detail the ionization, recombination, and cooling behind the shock, but its account of the flow dynamics is more approximate than in Lucy's model. One goal of a numerical simulation of this instability would be to determine what the likely character of the resulting nonlinear wind structure is, and whether it resembles either of these two pictures.

The instability of a line-driven flow has been recognized for a long time (Milne 1926; Lucy and Solomon 1970), and, given the above-cited observational evidence for extensive structure in line-driven winds, one may wonder why no such calculation of its nonlinear evolution has been done before now. The answer lies in the extreme difficulty of the problem. Since the instability occurs at scales near and below the Sobolev length, one cannot use the usual Sobolev approximation to calculate the line force. Instead one must, at least in principle, compute the force from detailed radiative transfer calculations for the several hundred strong lines important in driving the wind. This must be done repeatedly in time steps a fraction of the instability growth time over a much longer time scale of many wind expansion times. It

also must be done over a spatial scale of several stellar radii at a resolution smaller than a Sobolev length, which is typically only a few percent of a stellar radius. Finally, the calculation must accurately contend with possible nonmonotonic velocity variations more than a hundred times the thermal width of the driving lines!

Clearly, if we are to make progress despite these difficulties, it is essential to develop approximations to make the calculation more tractable. For this initial study, we have thus adopted what we consider to be the simplest possible model that still retains the basic physics of the instability. This model assumes a 1-D, spherically symmetric, isothermal stellar wind that is driven radially outward through absorption of a point source of continuum radiation by a fixed ensemble of isolated, pure-absorption lines. We thereby leave to future papers in this series consideration of such potentially important complications as a finite stellar disk, detailed energy and ionization balance, scattering line radiative transfer, and multi-dimensional flow. We do, however, derive the line force from detailed computation of the height and frequency dependence of the line absorption, rather than from the usual Sobolev approximation (Sobolev 1960; Lucy 1971; Castor 1974). This enables us to study how unstable perturbations on a scale near or below the Sobolev length grow beyond the linear regime. The results obtained so far seem to confirm that recurring shocks do form, but the specifics of both the shock formation and the shock structure are quite different from previous expectations.

The remainder of this paper is organized as follows. First (section II) we describe the radiation-hydrodynamics code used in our numerical simulations. Next (section III) we compare unperturbed wind models computed with this code with previous analytic, steady-state models based on the Sobolev approximation. (Results for time-dependent numerical models using the Sobolev approximation are presented in Paper I.) Then (section IV) we describe simulations of the nonlinear wind structure that arises from amplification of initially small-amplitude perturbations at the wind base. Finally (section V) we summarize our principal conclusions and outline directions for future work.

II. METHOD

In order to simulate the nonlinear evolution of this instability, we have recently developed a time-dependent radiation hydrodynamics code that numerically integrates a radiatively driven stellar wind model forward in time. In this section we outline how this code works; a more detailed description can be found in Paper I.

Let us first identify two principal difficulties in carrying out such a simulation. First, since the flow is known to be *physically* unstable, we must take special care to ensure that our numerical method is not also *numerically* unstable. Indeed, since the instability is strongest for perturbations *below* a Sobolev length, the method must be able to suppress, or at least control, the physical instability on scales near that of the numerical grid, lest the fluctuations associated with finite differencing become so amplified as to invalidate the basic assumption of small changes between grid points. At the same time, the suppression must not be so strong as to eliminate the instability we wish to study at scales near the Sobolev length. The second difficulty arises from the requirements of the radiative force computation; as already alluded to in the introduction, this must be accurate, reflecting the effects of possibly large nonmonotonic velocity variations over spatial scales a tiny fraction of a stellar radius, and yet efficient, allowing repeated computation over time steps a fraction of a wind expansion time.

In light of these difficulties, our approach has been to keep both the physical model and the numerical method as simple as possible. We thus assume a 1-D, spherically symmetric, isothermal flow that is driven radially outward through absorption of a point source of continuum radiation in a fixed ensemble of spectral lines. The hydrodynamical equations to be

integrated describe the conservation of mass density ρ ,

$$\frac{\partial \rho}{\partial t} + \frac{1}{r^2} \frac{\partial(\rho v r^2)}{\partial r} = 0, \quad (1)$$

and conservation of momentum flux density ρv ,

$$\frac{\partial \rho v}{\partial t} + \frac{1}{r^2} \frac{\partial(\rho v^2 r^2)}{\partial r} = -\frac{\partial P}{\partial r} - \rho g_* + \rho g_{rad}. \quad (2)$$

Here t and r are the time and radial position, v is the radial flow speed, and g_* is the effective stellar gravity (reduced by the effect of the radiative force on electrons). No explicit energy equation is currently treated, since the gas is assumed isothermal. We use the perfect gas law to evaluate the pressure P , assuming a fixed wind temperature T . Radiation provides the principal driving force for the flow, and so evaluation of the radiative acceleration, g_{rad} , plays a central role in the computation, as described below.

The spatial domain of our time-dependent wind model extends from a lower radius at $r_o = R_*$, the photospheric radius where the electron scattering optical depth is approximately unity, to an outer radius that ranges from $r = 2R_*$ to $r = 5R_*$, depending on the model. Initially, the boundary conditions for the hydrodynamic variables ρ and ρv were set as follows: at the lower boundary, we fixed ρ (and thus P), but allowed ρv to float by requiring only that its second spatial derivative vanish at the boundary; at the upper boundary, we allowed both ρ and ρv to vary, requiring only that the second derivatives of both quantities vanish. Later we experimented with more elaborate boundary conditions that constrain the Riemann invariants for the incoming characteristics. (See, e.g., Nakagawa and Steinolfson [1976].) At the lower boundary, we also implemented the form of boundary condition suggested by Hedstrom (1979) that is meant to minimize wave reflection. In practice we found that the earlier, simple boundary conditions and these more elaborate ones yielded quite similar results.

In calculating the radiative acceleration, g_{rad} , we assume pure attenuation in the driving lines, that the lines do not overlap, and that they have fixed opacities. As we will see, these are the assumptions that allow us to express the total force produced by all the lines as an integral, without the necessity for solving any equations of transfer; this results in an enormous savings in computer time. The force from a single such driving line with an opacity κ and at a frequency ν can be written as

$$g_{\nu, \kappa}(r) = \frac{\kappa \nu F_{\nu} \nu_{th}}{c^2} \int_{-\infty}^{\infty} dx \, l(x) \phi(x - \nu(r)/\nu_{th}) e^{-\tau(x, r)}, \quad (3)$$

where c is the speed of light, ν_{th} the ion thermal speed, x the thermal-unit frequency displacement from line center, and $\phi(x)$ the line profile function (assumed Doppler). The line optical depth $\tau(x, r)$ is measured outward from the base radius r_o (see eqn. (9) below), where the incident stellar flux is assumed to have a frequency distribution near the line that can be separated into a slowly varying continuum component F_{ν} and an incident line profile $l(x)$; we take this incident profile to be the transmission of a Schuster-Schwarzschild-type reversing layer (cf., Jefferies 1968, p. 30),

$$l(x) = e^{-\kappa \phi(x)/\sigma_c}. \quad (4)$$

The reversing layer thickness is taken to be that corresponding to continuum optical depth unity, and we have assumed that the continuum opacity σ_c is due only to electron scattering.

In a hot-star wind, there are a very large number of such lines, but since they are assumed not to overlap, the total force from all of them can be written quite simply as an integral over a line number distribution $N(\nu, \kappa)$ in frequency and opacity,

$$g_{rad}(r) = \int_0^\infty d\kappa \int_0^\infty dv N(v, \kappa) g_{v, \kappa}(r). \quad (5)$$

In this paper we shall assume (*cf.*, CAK, Abbott 1982) that the opacity number distribution defined by

$$N(\kappa) \equiv \int_0^\infty dv \left[\frac{vF_v}{F} \right] N(v, \kappa), \quad (6)$$

is given by the exponentially truncated power law,

$$N(\kappa) = \frac{1}{\kappa_o} \left[\frac{\kappa}{\kappa_o} \right]^{\alpha-2} e^{-\kappa/\kappa_{max}} \quad (7)$$

where α is the CAK power index ($0 < \alpha < 1$), κ_o is a constant related to the CAK force constant k (and set by the line list), and the cutoff at a maximum opacity κ_{max} is introduced here to enable us to limit the effect of very strong driving lines. (See section IIIa.) Absorption by this line ensemble of a point source of radiation with total flux F then yields the combined radiative acceleration,

$$g_{rad}(r) = \frac{\kappa_o^{1-\alpha} F \Gamma(\alpha) v_{th}^\alpha}{c} \int_{-\infty}^\infty dx \frac{\phi(x - v(r)/v_{th})}{(\eta(x, r) + 1/\kappa_{max} + \phi(x)/\sigma_c)^\alpha} \quad (8)$$

where Γ is the complete gamma function. (The choices that led to eqtns. [4] and [7] were dictated by the need to perform the integral over κ analytically.) We have introduced the profile-weighted mass column depth $\eta(x, r)$, related to the line optical depth $\tau(x, r)$ by

$$\begin{aligned} \eta(x, r) &= \frac{\tau(x, r)}{\kappa} \\ &= \int_{r_o}^r dr' \rho(r') \phi(x - v(r')/v_{th}). \end{aligned} \quad (9)$$

In our numerical computations we have found it advantageous to recast equation (8) as

$$\rho g_{rad} = \frac{-1}{r^2} \frac{d(r^2 P_{rad})}{dr}, \quad (10)$$

where

$$\begin{aligned} P_{rad} &\equiv \frac{-1}{r^2} \int dr' r'^2 \rho(r') g_{rad}(r') \\ &= -\frac{N_o F \Gamma(\alpha) v_{th}^\alpha}{(1-\alpha)c} \int_{-\infty}^\infty dx \left[\eta(x, r) + \frac{1}{\kappa_{max}} + \frac{\phi(x)}{\sigma_c} \right]^{1-\alpha} \end{aligned} \quad (11)$$

is the radial radiation pressure, apart from an additive term constant/ r^2 .

Since a flow driven by such a line-force is highly unstable, with the strongest growth for perturbations with a length scale smaller than a Sobolev length, $l \equiv v_{th}/(dv/dr)$ (Owocki and Rybicki 1984), there is a strong tendency to form small scale structure. In numerically simulating flows with such a tendency, an appealing idea is to use adaptive mesh methods, which refine the numerical grid as needed to resolve the evolving structure (Winkler et al. 1985). There are several reasons, however, why such methods are not best suited for this problem. First, their implicit time-stepping, which is required to keep size of the time step from getting very small as the grid becomes finer, would be both costly and difficult to implement for the relatively complicated radiative driving force considered here. Secondly, this extra cost could not be compensated by taking large time steps, since the time step would still be limited to an instability growth time, which decreases with decreasing scale of the structure. Finally, in a flow such this one in which the instability persists to the very smallest scales, these methods are subject to an "ultraviolet catastrophe": after each refinement of the mesh the instability produces structure of a yet-finer size, causing the refinement to be repeated indefinitely unless it is artificially limited at some minimum scale that one is willing to resolve.

Since limiting the minimum resolution scale is unavoidable anyway, we have chosen here the much simpler approach of keeping the spatial mesh fixed. In order to study instabilities that have their strongest growth at and below a Sobolev length l , we set the mesh size to be about $l/10$. The numerical integration method we have chosen uses staggered-mesh Eulerian hydrodynamics with an explicit time stepping that is operator split into separate Lagrangian and advection half-steps. (See Paper I.) In the Lagrangian half-step, the momentum flux density is updated according to the momentum sources, including that associated with the radiative force, and also including quadratic pseudo-viscosity to smooth shock fronts (Richtmyer and Morton 1979). In the advection step, the flow variables are re-mapped onto a fixed staggered mesh using monotonized piecewise-linear interpolation (van Leer 1977). After some experimentation, we have found that when this remapping is done using velocities derived from the old, *i.e.* non-updated, momentum flux density, the instability on the grid scale is suppressed, while that over several spatial zones near a Sobolev length is retained, as required. Arbitrary choices such as this are a necessary part of operator splitting schemes; further discussion of our choice of splitting will be found in Paper I. An alternative we tried and rejected was to locally enhance the pseudo-viscosity near steep rarefactions, which we found led to unphysical flow structures that were dominated by the artificial viscous force.

The term "staggered mesh" means that scalar quantities, such as the density or pressure, are referred to zone centers, while vector quantities, like momentum flux density or the radiative-force, refer to zone interfaces; this allows the equations of motion (1) and (2) to be approximated in terms of finite differences that are nominally second order in both time and space. In our staggered mesh hydro scheme, the (vector) radiative force at a zone interface is computed by equation (10) using differences between the (scalar) radiative stress from the neighboring zone centers, as computed from equation (11). This has proved to be more stable than a method based directly on equation (8), which is a great practical advantage.

Although greatly simplified compared to the real physical situation, the driving force computed from equations (9)-(11) retains the sensitive velocity dependence that gives rise to the strong instability. But because it is inherently nonlocal, it is much more complicated and more costly to evaluate than the usual body forces that are included in hydrodynamical simulations. At each time step, the radiative stress is calculated from trapezoidal rule evaluation of the double integral given by equations (9) and (11) over the fixed mesh of frequency and radius points. The nesting of the sums can quite easily be arranged to allow full vectorization, but this evaluation nonetheless dominates the computational cost. This cost increases with decreasing wind temperature as $T^{-3/2}$, owing to the need for a finer frequency mesh, smaller

spatial zones, and a smaller time step as the temperature is reduced; we thus normally assume a wind temperature T that is artificially enhanced by a factor of ten over the nominal radiative equilibrium value. (See section IIIa.)

The frequency mesh is chosen to resolve the lines with three frequency points per thermal width; the code dynamically adjusts the total number of frequencies to cover the velocity range of the wind, and typically uses $n_x = 150-250$ points. The spatial mesh is nominally set to $250 \text{ zones}/R_*$, which is sufficient to resolve the Sobolev length at a resolution of $\Delta r \approx l/10$; all results presented here remain qualitatively unchanged by either halving or doubling this nominal grid size. The time step is chosen to be a fixed fraction, usually 0.4, of the smallest Courant time $\Delta r/v$ over the grid, yielding a typical step size of $\Delta t \approx 10 \text{ s}$. As a specific example of computational cost, the nominal case of $n_r = 500$ and $n_x = 250$ requires about 0.5 CPU-sec per time step on a CRAY X-MP when the sums are properly vectorized. Hence about 1000 steps, or 10 Cray-min, are required to evolve this model by a single expansion time, $\tau_{\text{exp}} \equiv r/v \approx 2 \times 10^4 \text{ s}$. For models with finer spatial resolution, the cost increases as $1/(\Delta r \Delta t) \sim \Delta r^{-2}$.

III. RESULTS FOR AN UNPERTURBED WIND

a. Evolution from an Initial Condition Based on the Sobolev Approximation

Most previous models of radiatively driven stellar winds have used the Sobolev approximation to calculate the line force. In the present context, this can be viewed as assuming that the variation of the integrand in equation (9) is dominated by the Doppler shift of the line profile that occurs as the velocity v changes by a thermal speed v_{th} . Thus, over a Sobolev length scale $l \equiv v_{th}/(dv/dr)$, one assumes that the density is approximately constant at the value, $\rho(r') \approx \rho(r)$, and so can be moved outside the integral. Assuming further that the velocity increases monotonically with radius, one then can convert the variable of integration to co-moving frame frequency $x' \equiv x - v/v_{th}$. This makes it possible to evaluate the integrals in both equations (8) and (9) analytically, yielding the Sobolev line force,

$$g_{\text{Sob}}(r) = \frac{N_o F \Gamma(\alpha)}{(1-\alpha)c} \left[\frac{1}{\rho c} \frac{dv}{dr} \right]^\alpha \left[\frac{(1+\tau_{\text{max}})^{1-\alpha} - 1}{\tau_{\text{max}}^{1-\alpha}} \right], \quad (12)$$

where

$$\tau_{\text{max}} \equiv \frac{\rho \kappa_{\text{max}} c}{dv/dr}. \quad (13)$$

In the case of a pure power law line ensemble ($\kappa_{\text{max}} \rightarrow \infty$), the term in square brackets approaches unity. Equation (12) then takes exactly the simple analytic form originally derived by CAK, in which the force varies with the local velocity gradient as $g_{\text{CAK}} \sim (dv/dr)^\alpha$. Such Sobolev-theory, line-force expressions have proven extremely useful in constructing steady-state wind models. We have used this CAK force expression in our radiation-hydrodynamics code to show that, for a variety of initial conditions, time-dependent numerical calculations evolve asymptotically toward a steady-state that is nearly identical to the corresponding analytic CAK wind model (Paper I). This confirms the expectations of earlier linear analyses (Abbott 1980; Owocki and Rybicki 1984) that line-driven wind models based on the Sobolev approximation are hydrodynamically stable.

We now wish to compare these CAK models with results from numerical calculations using the more general force expression that does not use the Sobolev approximation (*cf.*, section II). For this, and all the numerical calculations in this paper, we choose a standard set of stellar parameters, listed in Table 1, that correspond to a typical O-star. Recall that, for

economy of calculation, we set the wind temperature to be ten times the nominal value given by radiative equilibrium. Even at this higher temperature the force due to radiation in most of the wind still dominates over that due to gas pressure, and so these models should be similar to what would be obtained from a more expensive calculation with a lower temperature. In particular, since the temperature has no effect on the CAK line force, the CAK model with this enhanced temperature is virtually identical to the one obtained with the usual assumption that wind temperature is near its radiative equilibrium value.

Figure 1 shows a comparison of the CAK line force g_{CAK} (dotted curve) with the more general absorption force g_{rad} (dashed curve) calculated from equations (9)-(11), using the same CAK wind model for the spatial variation of velocity (solid curve) and density. The difference (dash-dot curve) is small in the supersonic region, where Sobolev theory is valid, but quite substantial in the subsonic flow near the wind base, where the Sobolev approximation breaks down. This means that when the CAK analytic steady-wind solution is used as an initial condition in a numerical time-dependent wind calculation based on the more accurate line force, the flow is not steady, but evolves. The initial acceleration $\partial v / \partial t|_{t=0} = g_{rad} - g_{CAK}$ is largest in the subsonic region near the base, but then the disturbance created there propagates outward through the wind. This is illustrated in Figure 2, which shows the wind velocity versus radius at various times after the initial condition at $t = 0$. Note that the initial disturbance becomes greatly amplified, owing to the strong line-driven flow instability, and forms a pulse with a very steep rarefaction, or velocity rise.

Although very steep, these rarefactions are not discontinuities, but rather there is a small length scale of their leading edges that has a minimum value set by the maximum possible radiative force, which is that attained when all the lines are optically thin. However, in a CAK-type power-law line ensemble without an exponential cutoff this maximum possible force is infinite, and so the length scale can, in principle, approach zero. Indeed, this occurred in our calculations. This poses a serious problem, since it means that any finite-difference method, including adaptive mesh methods, must eventually fail to resolve the structure (*cf.* sec. II). Furthermore, since, unlike shock discontinuities, these rarefactions have an intrinsic structure, they cannot simply be spread with artificial viscosity, as is often done to resolve shocks. This would alter the nature of the radiative absorption within the rarefaction, leading, as we have found by numerical experimentation, to an overall flow structure that is quite unphysical.

In the present work, we have chosen simply to limit the steepness of the rarefactions by limiting the strength of the strongest driving line. Fortunately, this can be done without greatly altering the gross properties of the flow. In particular, steady-state, Sobolev-theory wind models analogous to CAK but with an exponential cutoff in the line distribution (*cf.*, eqn. (7)) have nearly the same CAK velocity law, and their mass loss rates are only slightly reduced, roughly in proportion to the reduction in the *number* of optically thick lines. After some experimentation, we have chosen here to use a cutoff of $\kappa_{max} = 10^{-3}\kappa_o$, which apparently makes the steepness of rarefactions manageable while only reducing the computed mass loss rates by about a third.

b. Asymptotic State of an Unperturbed, Absorption-Line-Driven Flow

Rather than concentrate any further on the detailed initial evolution of the wind, let us now consider the nature of the asymptotic state that the flow approaches after these initial disturbances propagate away.

i) Self-Excited Waves

Figure 3 shows the initial CAK velocity law as well as the velocity attained many flow times ($t > 10^5$ sec) after the CAK initial condition. The oscillation of the various curves, which give the velocity at various distinct times separated by 10^3 s, show that, while the wind has evolved to a much quieter state, it still is not steady. Instead, there remains an almost periodic train of self-excited waves that have persisted even in the absence of continuing explicit perturbations. These waves have so far resisted all our attempts to eliminate them. They seem to be a ubiquitous feature of the asymptotic wind state, independent of the precise initial condition, and showing no sign of decreasing in amplitude for as long as we have run the calculation, which in some cases has been more than a few times 10^6 s, or more than a hundred times a characteristic wind flow time.

The persistence of these self-excited waves is a puzzle because the instability in the supersonic portion of the wind has been shown to be of an "advective" type (Bers 1983; Owocki and Rybicki 1986), implying that any initial disturbance should eventually be carried away by the flow. It is still possible that the subsonic region contains "absolute" instabilities, for which the effect of an initial disturbance is not carried away. In this case, however, such disturbances should grow to nonlinear amplitude in the subsonic region, whereas the waves seen here have a very small amplitude ($\delta p/p \approx 10^{-5}$) interior to the sonic point.

Perhaps it is simply unreasonable to expect that such a numerical calculation could ever become entirely quiescent in the presence of such a strong instability, even though that instability is of the advective type. Numerical experiments we have done, however, indicate that the waves are largely unaffected by changes in either the spatial grid or the time step, contrary to what one expects for some of the most obvious sources of numerical noise. There is, however, one important exception: in the present case, with the right boundary at $r = 2R_*$, the waves repeat quite regularly with a period of about 5000 sec; but when this boundary is extended further outward, the regularity of this repetition appears to be markedly reduced. Since it is difficult to construct a completely transparent boundary condition, it is possible that the effect of the outer boundary is somehow propagated back to the wind base, despite the fact that the flow is supersonic. Perhaps this sets up a resonance that allows a small fraction of the wave energy generated from the instability of the supersonic wind to be recycled back to the subsonic wind base, where it causes the small fluctuations that are the source for more unstable waves. These ideas require further investigation.

ii) Comparison with Previous Steady-State Models

In the region where the self-excited waves are still linear the flow is very nearly a steady state. The mass loss rate differs from the CAK value (corrected for the line cutoff) by only a few percent ($\dot{M} \approx 0.95\dot{M}_{CAK}$); but Figure 3 shows that the velocity law deviates much more substantially from the CAK solution. In the supersonic portion of the wind, where the line force is nearly equal to the CAK force, the velocity parallels the CAK law; but in the subsonic and transonic regions, where the Sobolev approximation is poor, the two velocity laws diverge. Such marked differences from the Sobolev result are not seen in previous, non-Sobolev wind models based on co-moving frame calculations of the scattering line transfer (Weber 1981; Castor and Weber 1985; Pauldrach et al. 1986). Their appearance here may be a consequence of our approximations, in particular: 1) the higher assumed values for the thermal speed and for the ratio of the thermal speed to sound speed, which increases the deviation of the radiation force from the Sobolev value; 2) the use of a pure absorption model, which neglects the force due of scattered radiation; and 3) the associated use of an absorption-line boundary condition on the incoming flux, which keeps the radiative force small until the flow speed exceeds the line thermal speed. Further study on the role of these approximations will thus be needed

before one can ascertain the significance of the differences of the velocity law computed here from that derived from Sobolev models.

IV. EFFECT OF PERTURBATIONS AT THE WIND BASE

The self-excited waves described above are troublesome in that we do not completely understand their origin and cannot control their characteristics. However, since their base amplitude of $\approx 10^{-5}$ is probably much smaller than that of actual wave fluctuations in the atmospheres of these stars, we can simply overwhelm them by explicitly introducing an input wave flux whose characteristics are chosen to simulate various types of atmospheric fluctuations. In this paper, we confine ourselves to one specific form for such wave input, namely monochromatic sound waves incident at the lower boundary of the wind with a base amplitude of 1% and a period of 4000 sec, the latter being chosen to correspond roughly to the quasi-periodicity of the self-excited waves. A systematic study of the response to other types of wave input will be deferred to future work, although the results for a few other periods and amplitudes will be briefly discussed at the end of this section (IVh).

a. Resulting Spatial Structure at a Fixed Time

Figures 4 and 5 show snapshots of the wind structure resulting from such a 1% base density perturbation with a period of 4000 s. They plot the density, the velocity, and the radiation force, all as a function of radius from the wind base at a fixed time ($t = 10^5$ s) many wind flow times after the initial introduction of the waves. This is long enough so that all initial transient responses have died away, and so the resulting overall wind structure is very nearly periodic at the driving wave period. Figures 4 and 5 represent outcomes from separate computations that differ only in the location of the outer boundary radius, set to $r = 2R_*$ and $r = 4R_*$, respectively. Detailed comparison shows the structure to be almost identical over the common spatial range $r = 1-2R_*$. This contrasts with results for the self-excited waves, which were quite sensitive to the location of the outer boundary. In fact, it is interesting that the driven response shows little evidence of interference from the self-excited waves, indicating that the driving is sufficiently strong to lock the oscillations to the driving frequency. (This is not always the case, and one class of deterministic chaos arises in nonlinear oscillators that are driven at other than their characteristic frequencies; cf., Dubois [1987]).

Figures 4 and 5 clearly illustrate the large amplitude oscillations in velocity and density that result from the strong amplification of the 1% base perturbation by the line-driven flow instability. The high velocity parts of the wave, which have been Doppler shifted out the line shadow of intervening material, are more strongly driven by the line force, and so accelerate to still higher speeds. Note however that the density of this high velocity material tends to become very low. This tendency for the high speed part of the wave to become very rarefied is a dominant feature of these calculations that has many important consequences. For example, it greatly reduces the extinction of the stellar radiation by the high speed flow and so diminishes the effect of line shadowing on overlying, lower speed material. This can be verified in Figure 4 by comparing the variations of velocity and line force for the high speed part of a particular wavelet, say the one at $r \approx 1.35R_*$. As the velocity peaks, the line force declines smoothly rather than dropping abruptly, as it would if line shadowing played a dominant role. The radiation force on the back side of the wavelet is, in fact, quite significant, implying that the entire wave, and not just its front, is being driven as a whole.

Figure 6 explicitly illustrates this phase relationship between the velocity and density. It shows the radial evolution of the velocity-density phase difference, as computed by fitting the temporal variations of each quantity to a sinusoid at each radius. For now, let us focus only on the evolution in the inner region below $r \approx 2R_*$. In the subsonic region $r < 1.1R_*$, the

velocity and density are in phase, but in the supersonic wind at $r > 1.1R_*$, the phase abruptly shifts so that they are almost anti-correlated. In order to understand the reasons for this phase shift, we must now examine the way the waves introduced at the base propagate outward through the wind.

b. Nature of the Wave Propagation

The solid curve in Figure 7 shows the radial variation of the wave phase velocity, as computed by numerically differentiating the velocity phase shown in Figure 6. ($v_p = \omega / \text{Re}(k) = \omega dr / d\phi$.) The dashed curves show the expected phase velocity for the inward and outward modes of radiatively modified acoustic waves, as derived by solving a local linear dispersion equation (Abbott 1980; Owocki and Rybicki 1984) for k versus ω at each radius, using data from the numerical model. Note that the terms "inward" and "outward" here refer to the sense of propagation as viewed from a frame that is locally co-moving with the flow; when viewed from a frame fixed with the star, the phase velocity of the inward mode actually becomes positive above a sonic radius of $r \approx 1.1R_*$ (see lower dashed curve in Fig. 7), where advection by the flow carries the wave away from the star. The important point illustrated by Figure 7 is that near this same sonic radius, the computed wave undergoes a sudden mode switch. As a result, the outward-propagating sound waves generated in the subsonic region are transformed into inward-mode, radiative-acoustic waves in the supersonic wind. As shown by the linear stability analysis of Owocki and Rybicki (1984), such inward-mode waves are much more strongly amplified than the outward waves, and so they dominate the structure of the outer part of the wind. In particular, it is a fundamental property of such inward-mode waves that the velocity and density fluctuations are opposite in phase, and this provides the basis for understanding the origin of the results described above.

The basic cause of the mode switch itself can be understood as follows. In the subsonic part of the flow, where the radiative force is small, both the inward and outward modes correspond to the two modes of ordinary acoustic waves. However, in the supersonic part of the flow, the radiative force modifies the waves so that the inward (outward) mode propagates faster (slower), relative to the fluid, than ordinary acoustic waves (Abbott 1980). Thus as waves introduced into the subsonic flow propagate outward past the sonic point, they enter a region in which the propagation speed relative to the fluid is rapidly decreasing for the outward mode, but rapidly increasing for the inward mode. Because of the steep gradients in flow variables near the sonic point, the scale length for these changes is quite small. In fact, it is smaller than the wavelength of the assumed sound waves, implying a breakdown in the usual WKB approximation for the propagation of waves through a weakly stratified flow. The behavior of waves in such a non-WKB region is complicated, but the usual effect is a mixing of the eigenmodes found in the local analysis. Such non-WKB mode mixing is thus most probably the cause for the mode switch observed here.

Since this mode-switching is a consequence of the steepness of the transonic flow in such an absorption-line-driven wind model, the question arises as to what degree the wind structure computed here is sensitive to the limitations of this absorption model (*cf.*, section IIIb). In particular, if proper treatment of scattering line transfer were to reduce the steepness of the velocity, then such non-WKB mode switching might also be greatly reduced. Nonetheless, because the inward-mode wave is much more unstable (Owocki and Rybicki 1984), it should still ultimately dominate the wind structure even if the mode mixing were very slight. Results presented here that stem from the inward-mode nature of the waves, or from the associated opposite phase relationship for density and velocity variations, thus should not be qualitatively changed by including such additional effects, although this must still be tested by a detailed calculation.

c. Temporal Growth of the Wave

It is of interest to find the amplitude at which the computed growth of the wave shows a significant deviation from that predicted by a linear analysis. In the linear regime the velocity amplitude should grow according to $\Delta v \sim \exp(\int dt \Omega)$, where, for the present value of α (0.7), the growth rate for very short scale ($\lambda \ll l$) perturbations is given by (see Owocki and Rybicki 1984, eqtns. (52)-(54)) $\Omega \approx 2.7v/l = 2.7(v/v_{th})(dv/dr)$. Since in the supersonic wind the waves move at nearly the flow velocity, we then have $\Delta v \sim \exp(\int dr \Omega/v) \sim \exp(2.7v/v_{th})$. Thus the accumulated number of e-folds expected from linear theory is just proportional to the mean flow velocity.

In Figure 8 the computed wave velocity amplitude, Δv , is plotted against the temporally averaged flow velocity, $\langle v \rangle$; the linear variation over several decades on these semi-log axes shows that the computed amplitude does indeed vary in this way. The smaller slope (*i.e.*, growth rate) for the computed waves can be attributed to the fact that their wavelength is longer than the Sobolev length, and so they have a lower growth rate than the very short waves assumed in the above linear theory estimate. It is striking, however, that the linear relationship holds to the large velocity amplitude $\Delta v \approx 500 \text{ km/s}$. This is more than an order of magnitude greater than a thermal speed, and a few times the velocity amplitude $\approx 150 \text{ km/s}$ at which the velocity becomes nonmonotonic.

Apparently, expected nonlinear effects, like line shadowing, have little effect in slowing the growth. This is probably because the high velocity material has a very low density, and so allows much of the stellar radiation to pass through and drive the back side of the wave. Since the whole wave, and not just the front, is driven together, there is no strong *dynamical* effect to cause the growth to saturate. Eventually, of course, the simple *kinematic* effect of fast material running into slower material forces the wave to steepen, slowing the growth; but this does not occur until the wave steepening time exceeds the instability growth time, at a highly nonlinear velocity amplitude of several hundred kilometers per second.

d. Formation of Shocks and Dense Shells

The shocks that result from this kinematic wave steepening are also quite different from what had been anticipated. Again, this is due to the fact that the high velocity part of these inward-mode waves has a very low density. As these waves steepen, they naturally give rise to a *reverse* shock, across which this very high-speed, rarefied material is compressed and decelerated to become part of a slower, very dense *shell* (*cf.* Fig. 4). Of course, like the inward-mode waves, these reverse shocks still propagate away from the star, but only because they are being advected outward by the supersonic flow. Their structure is in many ways opposite that of the *forward* shocks envisioned in earlier heuristic models (Lucy 1982b; Krolik and Raymond 1985; Abbott 1988), in which a fast, dense, radiatively driven flow rams into

slower, less dense, ambient material that is thereby accelerated and compressed across the forward shock. The key difference is that a forward shock *accelerates* slow material while a reverse shock *decelerates* fast material. Figure 4 shows that a forward shock does form here on the outer edge of the dense shell, but it is much weaker than the reverse shock. The net result is thus not just one, but a pair of shocks per wavelet.

The *dynamics* of the shock structure here is also quite different from that envisioned earlier. In previous forward-shock models the ambient pre-shock wind is only weakly driven because of line-shadowing by the underlying, dense, post-shock flow. Conversely, in the present reverse shocks, the fast, rarefied pre-shock flow is strongly driven, but because of its very low density, there is little line-shadowing of the overlying post-shock material in the dense shell. However, self-absorption within the dense shell itself does cause the force to decrease abruptly at the shock (see Fig. 4), much as in the earlier line-shadowed picture. (In fact, the variation of the force becomes flat-topped, in marked contrast to the smooth force decline that was characteristic of the flow before formation of shocks; *cf.* section IVa above). But even so, the reduction of line shadowing is still very important because it means that material outside the shell can be radiatively driven once its flow speed exceeds that of the relatively slow shell; it does not have to be accelerated out of the shadow of the previous high speed, low density flow.

It is worth noting that the nature of this shock structure actually helps justify, *a posteriori*, our neglect of a detailed ionization balance. Krolik and Raymond (1985) argue that the ionization of driving ions in the radiatively driven post-shock flow provides a natural self-regulation mechanism that limits the maximum strength of the shock. In the present case, however, such ionization effects are likely to play a less direct role because it is the radiative force on pre-shock, not post-shock, gas that drives the strong shock. Of course, it is still possible that more subtle effects cause the ionization balance to be dynamically important, but this will require a detailed calculation to determine.

e. Interaction of the Shells and Shocks

Let us now consider how this structure evolves over a larger spatial scale. Figures 9 (a) and (b) show the extrema of the density and velocity that occur at each radius during a wave period. Both the velocity and density show their maximum amplitude fluctuation at $r \approx 1.6R_*$, the location of initial formation of the shocks and shells. Above this radius, the fluctuation amplitudes then decline until $r \approx 2.3R_*$, where the density minimum shows an abrupt jump of more than two orders of magnitude. This radius of minimum density contrast thus seems to divide the flow into two quite distinct regions.

To see what is occurring at this radius, let us return attention to the snapshots of the flow structure shown in Figure 5. Since the wind structure is periodic, the spatial variation from wavelet to wavelet (or shell to shell) can be used to track the temporal evolution of a given wavelet (or shell) from period to period. Following in this way the sequence of three dense shells from $r \approx 1.4R_*$ to $r \approx 2R_*$, we can see that, because the shells are bounded by forward and reverse shocks, they tend to expand as they are advected outward. Figure 5 then shows that, at a radius of $r \approx 2.3R_*$, the outer edge of one shell overruns the inner edge of the next higher shell. This fills the rarefied region between the shells, resulting in the abrupt jump in minimum density shown in Figure 9(a). It also leads to the formation of a series of secondary shells that, superficially, appear quite similar to the originals.

Figure 6 shows that this shell interaction further results in a temporary decline in the velocity-density phase difference to about 90° . Both this and the increase in the intershell density mean that the highest velocity material in the post shell-interaction region has quite a high density, high enough to shadow the flow above from the stellar radiation; the subsequent

evolution of the flow above the interaction height of $r \approx 2.3R_*$ thus becomes purely hydrodynamic, with the radiative force no longer playing any role. In fact, the computed flow in this region somewhat resembles that observed in the distant solar wind, where similar shells and shocks form from the interaction of fast and slow wind streams (Pizzo 1986). In both cases, repeated shell interactions, each of which causes an incremental decrease in the shock amplitude, eventually lead to a smoothing of the wind.

Finally, we note that the terminal flow speed reached in the distant wind after smoothing of the shocks and shells is within a few percent of that predicted by the CAK model. Furthermore, the time-averaged mass loss rate is likewise very nearly the same as the CAK value (corrected for the reduction in the maximum line strength). Remarkably, all the extensive structure that arises in the acceleration region of the wind has apparently little net effect on its gross properties far from the star.

f. Structure with Respect to Mass

It is instructive to view the same velocity structure as Figure 5 in terms of a Lagrangian rather than an Eulerian spatial coordinate. Figure 10 thus shows this structure plotted versus the total mass above the wind base, in units of the mass lost by the star in one period. Note the sharp rarefaction, or step-like velocity jump, at a mass of $m \approx 3$; this illustrates the runaway character of the line-driven instability: one fluid parcel that is initially flowing slightly faster is strongly accelerated, while its near neighbor, initially flowing only slightly more slowly, is hardly accelerated at all. Note also the spike-like character of the rarefaction/shock pairs at $m \approx 4$ and $m \approx 5$, which illustrates how very little material is actually contained in the high velocity parts of the wave with $v > 1500$ km/s. Most of the mass seems instead to collect at a velocity of about 1200 km/s, and this suggests that such a wind structure might exhibit interesting spectral features, as will be described next.

g. Implications for Interpreting Observational Signatures of Wind Structure

It is natural to ask how the wind structure derived here compares with that inferred from the observations discussed in the introduction. Although a detailed comparison is beyond the scope of the present paper, let us consider the likely consequences of the computed structure for the interpretation of the observations in each spectral region.

1. Infrared and Radio

Recall that the observed infrared thermal emission from these winds is often larger than expected from a smooth wind with the mass loss rate inferred from radio or UV, perhaps reflecting a clumpiness that increases the mean square density, and hence the emission measure, of the regions of infrared emission. Figure 11 shows the radial variation of the clumping factor, $\langle \rho^2 \rangle / \langle \rho \rangle^2$, for the driven wave model discussed above. The typical magnitude of ≈ 5 for this quantity corresponds roughly with that needed to explain the infrared enhancement (Abbott et al. 1984). Interestingly, clumping occurs in two peaks that correspond to the regions of peak amplitude in the primary and secondary shells near $r \approx 1.6R_*$ and $3.0R_*$, respectively. The smaller magnitude of the outer peak reflects a general decline of the density contrast (*cf.* Fig. 9(a)) that should continue as the flow reaches large radii. Thus thermal radio emission, which also scales with the mean square density but which arises from a much larger radius, should not be much enhanced. Particles accelerated near the shocks at smaller radii may give rise to a non-thermal radio emission (White 1985), but since these levels are quite optically thick in the radio, it is unclear whether that this could produce sufficient emergent flux to explain the non-thermal radio emission observed from several hot-stars.

2. X-ray

The strength of the shocks computed here seem to correspond qualitatively to what would be required to produce the luminosity and spectral properties of the observed soft X-rays. For example, the computed shock velocity-jumps range from $\Delta V = 500$ km/s to 1000 km/s (see Figure 4), implying post-shock temperatures in the range 10^6 K to 10^7 K, much as inferred from the observed X-ray spectra. The energy dissipated in such a shock (which in the present spherically symmetric models is assumed to extend all around the star) is roughly $E = 2\pi r^2 \rho (\Delta V)^3$. We take, from Figure 4, $\rho \approx 10^{-16}$ g/cm³ for the mass density at $r \approx 1.6R_*$, immediately preceding the shock velocity jump of $\Delta V \approx 700$ km/s, with the result $\dot{E} \approx 2 \times 10^{33}$ erg/s. Assuming that there are a few such shocks present at any one time, and that a substantial fraction of the energy from each is emitted as X-rays, this would be more than adequate to provide the observed X-ray luminosity, which, for a star with the assumed bolometric luminosity of $L_{Bol} = 6 \times 10^5 L_O$, would be roughly $L_x \approx 10^{-7} L_{Bol} \approx 2 \times 10^{32}$ erg/s. However, both this observational quantity and the above theoretical estimate are quite uncertain because of the large correction for X-ray absorption within the wind. Thus more detailed calculation of the both production and transport of the X-rays will be needed to determine how well the properties of this computed wind structure agree in detail with X-ray observations.

3. Ultraviolet

As mentioned above (*cf.*, section IVf), the general properties of the distribution of velocity with mass suggest that the UV lines formed in such a flow should exhibit interesting spectral features. Consider the *absorption* profile that would occur for a moderately strong line that is optically thick, but unsaturated in the wind. Figure 12 shows the residual flux vs. wavelength (measured from line center in velocity units) at four phases of the wave period in the standard, perturbed wind model discussed above. At low velocities ($v \approx 300$ km/s) the absorption varies greatly with phase, but at two discrete higher velocities, corresponding to the velocities ($v \approx 900$ km/s and 1250 km/s) of the primary and secondary dense shells shown in Figure 5, the absorption is strongly enhanced at all four phases. Although this ignores, for computational simplicity, the emission component that exists in actual scattering lines, we note that such emission should be quite smooth in frequency, since it arises from the cumulative contribution of material over a large volume with a wide range of line-of-sight velocities (Castor and Lamers 1979). The absorption part of a P-Cygni profile synthesized for a scattering line in this computed wind model is thus also very likely to show narrow absorption features like those in Figure 12. Since these features persist at all phases of the wave, they should even appear in profiles that are time-averaged over a wave period, or spatially averaged over lines of sight that have oscillations with various phases. The computations presented here thus provide a reasonable basis for understanding the common appearance of such narrow absorption components in UV line spectra observed with *IUE*. Note further that although the individual wind structures propagate outward through the wind, their periodicity means that the narrow absorption components that they cause can persist for many wind expansion times, and this may help explain the persistence of some such features in *IUE* spectra made months or even years apart.

Finally, we note that, because of the net backscattering that is likely to result from the highly non-monotonic velocity fields computed here, the absorption troughs of very strong UV lines formed in these flows are likely to be "black" (Lucy 1982a), much as is commonly observed.

h. Results for Other Amplitudes and Periods

We have also computed models for a limited selection of other amplitudes and periods for the driving perturbations. The results show that reducing or increasing the amplitude from the earlier value of 1% yields results qualitatively similar to those shown above, except that the waves reach nonlinear amplitude at a slightly higher or lower radius, as would be expected. Interestingly, the wind structure arising from perturbations with base amplitude greater than about 10% tends to be much less regular, showing signs of chaotic behavior that is often characteristic of strongly driven nonlinear systems.

When the period is reduced by a factor of two to 2000 sec, the same periodic shock structure seen before occurs, except that both the amplitude of the shocks and the spatial scale over which they form and interact are reduced by roughly the same factor of two. Because these higher frequency waves have a smaller wavelength, they have a shorter kinematic steepening time and so steepen at a smaller amplitude and a lower radius than before. Likewise, the distance between the dense shells is less and so the shocks and shells also begin to interact at a lower height.

The results when the period is *increased* by a factor of two cannot be explained so simply. Although the wind structure is still temporally periodic at the wave driving period, it is no longer so spatially regular. It thus appears that the driving at this period is above some critical wind response period that allows simple wave propagation. This critical period is apparently related to the characteristic period of ≈ 5000 s for the self-excited waves, but we have not yet been able to determine its exact nature or origin. It is much lower than the acoustic cutoff period, which in this case is $4\pi a/g \approx 47,000$ sec, and corresponds roughly to the period associated with radiative amplification, which is $v_{th}/g_{rad} \approx l/v \approx 2500$ sec. We also find qualitatively similar, irregular spatial structure for the still longer periods (~ 10 -20 hours) that are characteristic of nonradial pulsations observed in these stars.

V. CONCLUSIONS

In this paper we have presented results from numerical simulations of the nonlinear evolution of line-driven flow instabilities in an idealized model of a radiatively driven stellar wind. This model assumes a spherically symmetric isothermal stellar wind driven radially outward through absorption of a point source of continuum radiation by a fixed ensemble of isolated, pure-absorption lines. Our results are summarized as follows:

1. In the absence of perturbations, such a time-dependent wind model asymptotically becomes nearly steady, with a mass loss rate similar to the CAK steady-state model, but with a much steeper velocity law.
2. This unperturbed wind never becomes completely steady, however, since there persist near the subsonic wind base small amplitude fluctuations that are amplified by the line-driven instability into nonlinear waves in the supersonic flow.
3. The strong velocity dependence of the line force leads to the formation of very steep rarefaction waves. Their steepness, and hence the computational expense of resolving them, can be limited by limiting the strength of the strongest driving line.
4. Outward-propagating sound waves incident at the base of the wind change in character, because of the breakdown of the WKB approximation, in the region of most rapid acceleration just outside the sonic point, and become inward-mode radiative-acoustic waves for which the fluctuations in density and velocity are nearly opposite in phase.
5. The low density of the high-speed part of such waves diminishes the effect of line shadowing so that the wave growth follows the rate predicted by linear theory well into the nonlinear regime, when kinematic effects cause the waves to steepen, thereby saturating

their growth.

6. As they steepen, such inward-mode waves form very dense shells, bounded on the inner edge by a strong reverse shock that connects to the high-speed, rarefied flow below, and bounded on the outer edge by a weaker, forward shock that connects to slower, moderate density wind. Eventually the shells expand and interact to form a secondary shell structure in which the high-speed flow has a high enough density to shield the outer wind from any further radiative driving.
7. This computed wind structure is qualitatively consistent with that needed to explain various observational properties of these stars: enhanced infrared emission resulting from the wind clumpiness, non-thermal radio emission from particles accelerated near shocks, soft X-ray emission from shock-heated gas, black absorption troughs in strong UV lines due to the net backscattering of the highly nonmonotonic velocity, and narrow absorption components in UV lines arising from absorption by the dense shells.
8. Despite the presence of extensive structure, the gross properties of the wind, such as the average mass loss rate and terminal flow speed, are quite similar to those derived by steady-state wind models like CAK.

The principal conclusion we draw from these results is that the line-driven flow instability should, as expected, lead to extensive formation of shocks within a radiatively driven wind, but the nature of these shocks and the associated wind structure may be quite different from what had been anticipated. In particular, the fastest, most strongly driven flow may be highly rarefied, not dense, and the strong shocks that form may be of the reverse, not the forward, type. These results are likely to have important consequences for how one interprets the observational evidence for structure in these winds.

A primary goal for future work will be to develop techniques for making quantitative comparisons with available observations, particularly in ultraviolet lines and X-rays. We also hope to improve this model by progressively relaxing the present simplifying assumptions. In the meantime, we must emphasize that inclusion of these additional effects may significantly alter the computed wind structure, and so modify the present results. In any case, the numerical simulations presented here provide an intriguing glimpse of some subtle nonlinear aspects of the dynamical interplay between matter and radiation in the highly unstable radiatively driven stellar winds. The methods developed should also provide a basis for the more complete studies to come.

Acknowledgements

The computations described here were performed on Cray supercomputers at the National Magnetic Fusion Energy Computer Center, the Lawrence Livermore National Laboratory, and the San Diego Supercomputer Center. This work was performed in part under the auspices of the U. S. Department of Energy by the Lawrence Livermore National Laboratory under Contract No. W-7405-ENG-48, and was partially supported by an Institutional Research and Development grant from L. L. N. L. S.P.O. also acknowledges partial support from NSF grant AST 86-11824 and NASA grant NAG-8-613.

References

- Abbott, D.C. 1978, *Ap. J.*, **225**, 893.
Abbott, D.C. 1980, *Ap. J.*, **242**, 1183.
Abbott, D.C. 1982, *Ap. J.*, **259**, 282.
Abbott, D.C., Telesco, C.M., and Wolff, S.C. 1984 *Ap. J.*, **279**, 225.

- Abbott, D.C. 1988, in *Solar Wind VI*, ed. V.J. Pizzo, NASA Conference Proceeding, in press.
- Abbott, D.C. Biegging, J.H. and Churchwell, E. 1981, *Ap. J.*, **250**, 645.
- Abbott, D.C. Biegging, J.H. and Churchwell, E. 1984, *Ap. J.*, **280**, 671.
- Bers, A. 1983, in *Handbook of Plasma Physics, Volume 1: Basic Plasma Physics I*, A.A. Galeev and R.N. Sudan, eds. (Amsterdam: North-Holland), p. 451.
- Carlberg, R.G., 1980, **241**, 1131.
- Cassinelli, J.P. 1979, *Ann. Rev. Astr. Ap.*, **17**, 275.
- Cassinelli, J.P. and Olson, G.L. 1979, *Ap. J.*, **229**, 304.
- Cassinelli, J.P. and Swank, J.H. 1983, *Ap. J.*, **271**, 681.
- Castor, J.I. 1974, *M.N.R.A.S.*, **169**, 279.
- Castor, J.I., Abbott, D.C., and Klein, R.I. 1975, *Ap. J.*, **195**, 157 (CAK).
- Castor, J.I., and Lamers, H.J.G.L.M. 1979, *Ap. J. Supp.*, **39**, 481.
- Castor, J.I., and Weber, S.V. 1985, unpublished.
- Castor, J.I., Owocki, S.P., and Rybicki, G.B. 1988, in preparation (Paper I).
- Dubois, M. 1987, in *Physics of Chaos and Systems Far from Equilibrium*, M. Duong-Van, ed., published as *Nuclear Physics B (Proceedings Supplement)*, **2**, (Amsterdam: North-Holland), p. 339.
- Harnden, F.R., Branduardi, B., Elvis, M., Gorenstein, P., Grindlay, J., Pye, J.P., Rosner, R., Topka, K., and Vaiana, G.S. 1979, *Ap. J. (Letters)*, **234**, L51.
- Hedstrom, G.W., 1979, *J. Comp. Phys.*, **30**, 222.
- Henrichs, H.F., Hammerschlag-Hensberge, G., Howarth, I.D., and Barr, P. 1983, *Ap. J.*, **268**, 807.
- Henrichs, H.F. 1984, 4th European *IUE* Conference (ESA SP-218), p. 43.
- Jeffries, J.T. 1968, *Spectral Line Formation*, (Waltham, Mass.: Blaisdell).
- Krolik, J. and Raymond, J.C. 1985, *Ap. J.*, **298**, 660.
- Lamers, H.J.G.L.M., and Morton, D.C. 1976, *Ap. J. Suppl.*, **32**, 715.
- Lamers, H.J.G.L.M., Gathier, R., and Snow, T.P. 1982, *Astron. Astrophys.*, **258**, 186.
- Lucy, L.B. 1971, *Ap. J.*, **163**, 95.
- Lucy, L.B. 1982a, *Ap. J.*, **255**, 275.
- Lucy, L.B. 1982b, *Ap. J.*, **255**, 286.
- Lucy, L.B. and Solomon, P.M. 1970, *Ap. J.*, **159**, 879.
- MacGregor, K.B., Hartmann, L., and Raymond, J.C. 1979, *Ap. J.*, **231**, 514.
- Martens, P. 1979, *Astron. Astrophys.*, **75**, L7.
- Milne, E.A. 1926, *M.N.R.A.S.*, **86**, 459.
- Morton, J.M. 1967, *Ap. J.*, **150**, 535.
- Mullan, D.J. 1984a, *Ap. J.*, **283**, 303.
- Mullan, D.J. 1984b, *Ap. J.*, **284**, 769.
- Mullan, D.J. 1986, *Astron. Astrophys.*, **165**, 157.
- Nakagawa, Y. and Steinolfson, R.S. 1976, *Ap. J.*, **207**, 296.
- Owocki, S.P. and Rybicki, G.B. 1984, *Ap. J.*, **284**, 354.
- Owocki, S.P. and Rybicki, G.B. 1985, *Ap. J.*, **299**, 265.
- Owocki, S.P. and Rybicki, G.B. 1986, *Ap. J.*, **309**, 127.
- Pauldrach, A., Puls, J., and Kudritzki, R.P. 1986, *Astr. Ap.*, **164**, 86.
- Pizzo, V.J. 1986, *Adv. Space Res.*, **6**, 353.
- Prinja, R.K., and Howarth, I.D. 1986, *Ap. J. Supp.*, **61**, 357.
- Prinja, R.K., and Howarth, I.D. 1988, *M.N.R.A.S.*, in press.
- Prinja, R.K., Howarth, I.D., and Henrichs, H.F. 1987, *Ap. J.*, **317**, 389.
- Richtmyer, R.D. and Morton, K.W. 1967, *Difference Methods for Initial Value Problems*, 2nd ed. (New York: Wiley-Interscience).
- Seward, F.D., Forman, W.R., Giacconi, R., Griffith, R.B., Harnden, F.R., Jones, C., and Pye,

- J.P. 1979, *Ap. J. (Letters)*, **234**, L51.
- Sobolev, V.V. 1960, *Moving Envelopes of Stars* (Cambridge: Harvard University Press).
- van Leer, B. 1977, *J. Comp. Phys.*, **23**, 276.
- Waldron, W.L. 1984, *Ap. J.*, **282**, 256.
- Weber, S.V. 1981, *Ap. J.*, **243**, 954.
- White R.L. 1985, *Ap. J.*, **289**, 698.
- Winkler, K.A., Norman, M.L., and Mihalas, D. 1985, in *Multiple Time Scales*, J. Brackbill and B. Cohen, eds. (New York: Academic Press).

Table 1: Model Parameters

| <u>Quantity</u> | <u>Symbols</u> | <u>Value</u> |
|-----------------------|------------------------|--|
| Mass | M_* | $50 M_\odot$ |
| Luminosity | L_* | $6.8 \times 10^5 L_\odot$ |
| Radius | R_* | $20 R_\odot$ |
| Effective Gravity | g_* | 2100 cm/s^2 |
| Effective Temperature | T_* | $37,000^\circ\text{K}$ |
| Wind Temperature | T | $370,000^\circ\text{K}$ |
| Thermal Speed | V_{th} | 40 km/s |
| Sound Speed | α | 80 km/s |
| Opacity Constant | κ_0 | $2270 \text{ cm}^2/\text{g}$ |
| CAK Power Index | α | 0.7 |
| CAK Mass Loss Rate | \dot{M}_{CAK} | $5.6 \times 10^{-6} M_\odot/\text{yr}$ |
| CAK Terminal Speed | $V_\infty(\text{CAK})$ | 1240 km/s |
| Driving Amplitude | A | 0.01 |
| Driving Period | P | 4000 sec |

Authors' Addresses:

Stanley P. Owocki
Bartol Research Institute
University of Delaware
Newark, DE 19711

John I. Castor
Lawrence Livermore National Laboratory
Mail Code L-23
Livermore, CA 94550

George B. Rybicki
Center for Astrophysics
60 Garden St.
Cambridge, MA 02138

Figure Captions:

1. Velocity and line-force per unit mass in a CAK line-driven wind model based on the Sobolev approximation. The force obtained from the CAK/Sobolev formula is compared with that computed from eqtns. (9)-(11) without resort to the Sobolev approximation. The difference shows the initial evolution of a time-dependent, non-Sobolev wind model when the CAK solution is used as an initial condition. The assumed stellar parameters are those given in Table 1.
2. Velocity versus radius at various times t after the CAK initial condition at $t = 0$. The initial adjustment of the subsonic region is quickly amplified into a steep rarefaction wave by the line force.
3. Wind velocity a long time ($> 10^5$ sec) after the CAK initial condition, when initial pulses like those shown in Fig. 2 have propagated away. Although there are no explicit perturbations, the wind state attained is not steady because of the persistence of small fluctuations at the base that are amplified into self-excited waves in the wind. The model is the same as in Fig. 2, except that the maximum strength of the driving lines has been limited in order to limit the steepness of rarefactions.
4. Density, velocity, and radiative force per unit mass, as functions of radius in units of R_* from the wind base to the right boundary at $r = 2R_*$. The curves represent a snapshot of the spatial structure at a fixed time ($t = 10^5$ s) long after the introduction of a sinusoidal, base-density perturbation of period 4000 s and amplitude 1% into the unperturbed model shown in Fig. 3.
5. Same as Fig. 4, but for a model with the right boundary extended to a radius of $r = 4R_*$.
6. Radial variation of the velocity-density phase difference in degrees. Note the abrupt shift near the sonic radius $r \approx 1.1R_*$.
7. Radial variation of phase velocity (solid curve) of the computed wave compared with the flow velocity (dot-dash curve), and with the phase velocities of inward and outward radiative-acoustic waves (dashed curves), obtained by solving a local, linear dispersion equation at each radius using coefficients derived from the numerical model.
8. Semi-log plot of the driven wave velocity amplitude vs. the temporally averaged flow velocity. Note that the growth remains exponential, as expected from linear theory, up to a highly nonlinear amplitude of $\Delta v \approx 500$ km/s.
9. Radial variation of the extrema in (a) density (plotted as the natural logarithm of the density over time-averaged density) and in (b) velocity, taken over the wave period. The large jump in minimum density at $r \approx 2.3R_*$ corresponds to the interaction of dense shells.
10. Velocity in same wind model as Figs. (4)-(9), but versus mass above stellar wind base, in units of wind mass lost in a wave period. Note the steepness of the rarefaction at a mass of $m \approx 3$ and the spike character of the rarefaction/shock pairs at $m \approx 4$ and $m \approx 5$.
11. Radial variation of the density "clumping factor", defined as the ratio of the mean square density over the square of the mean density. The two maxima correspond to the regions of primary and secondary shell formation discussed in the text.
12. Absorption line profiles (omitting emission) of a typical, strong line for four phases of the driving wave. The persistent features at $v \approx 900$ km/s and $v \approx 1300$ km/s, which arise respectively from absorptions by the primary and secondary dense shells, are reminiscent of the narrow absorption components that are commonly observed in UV lines from hot stars.

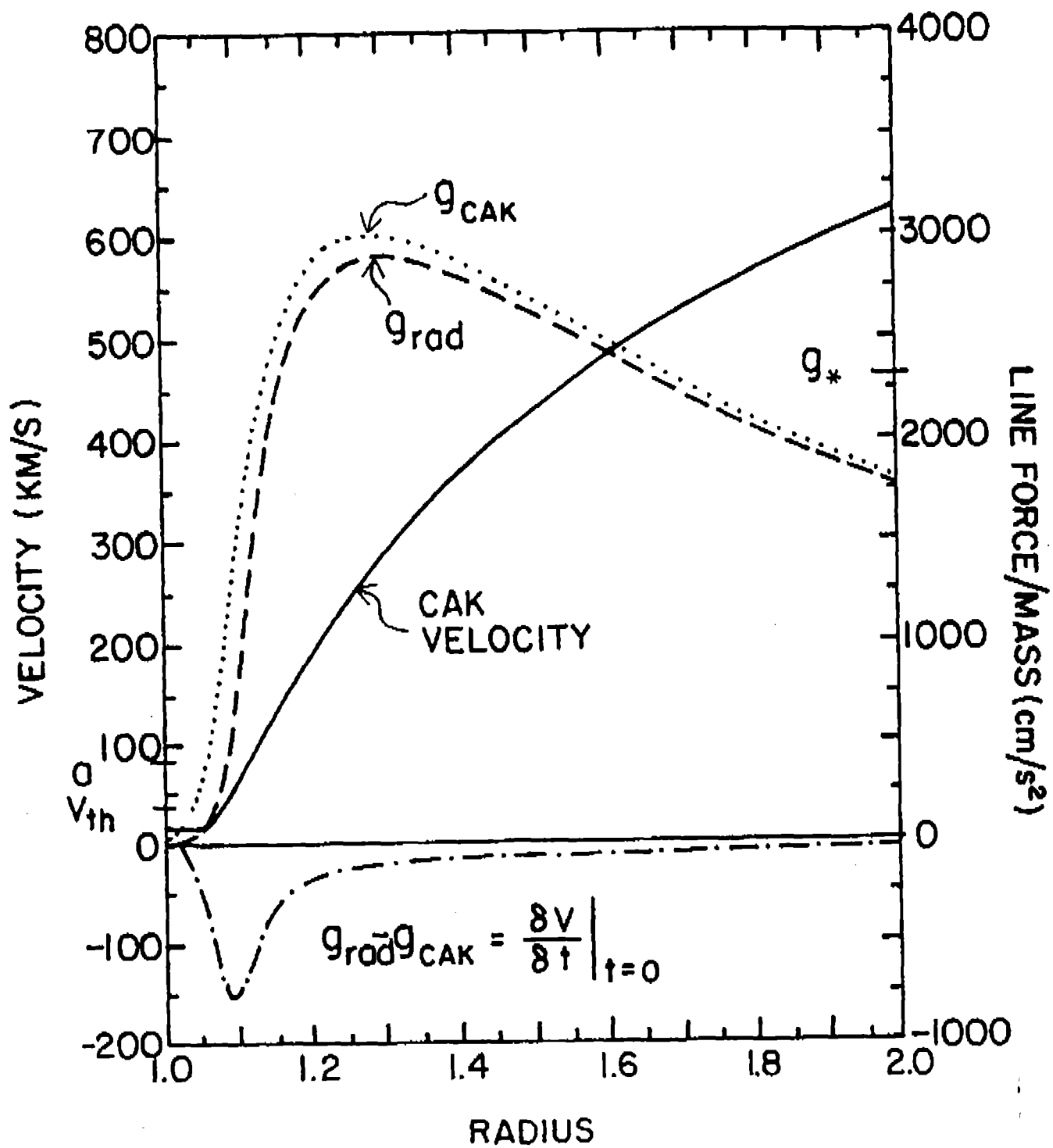


FIGURE 1

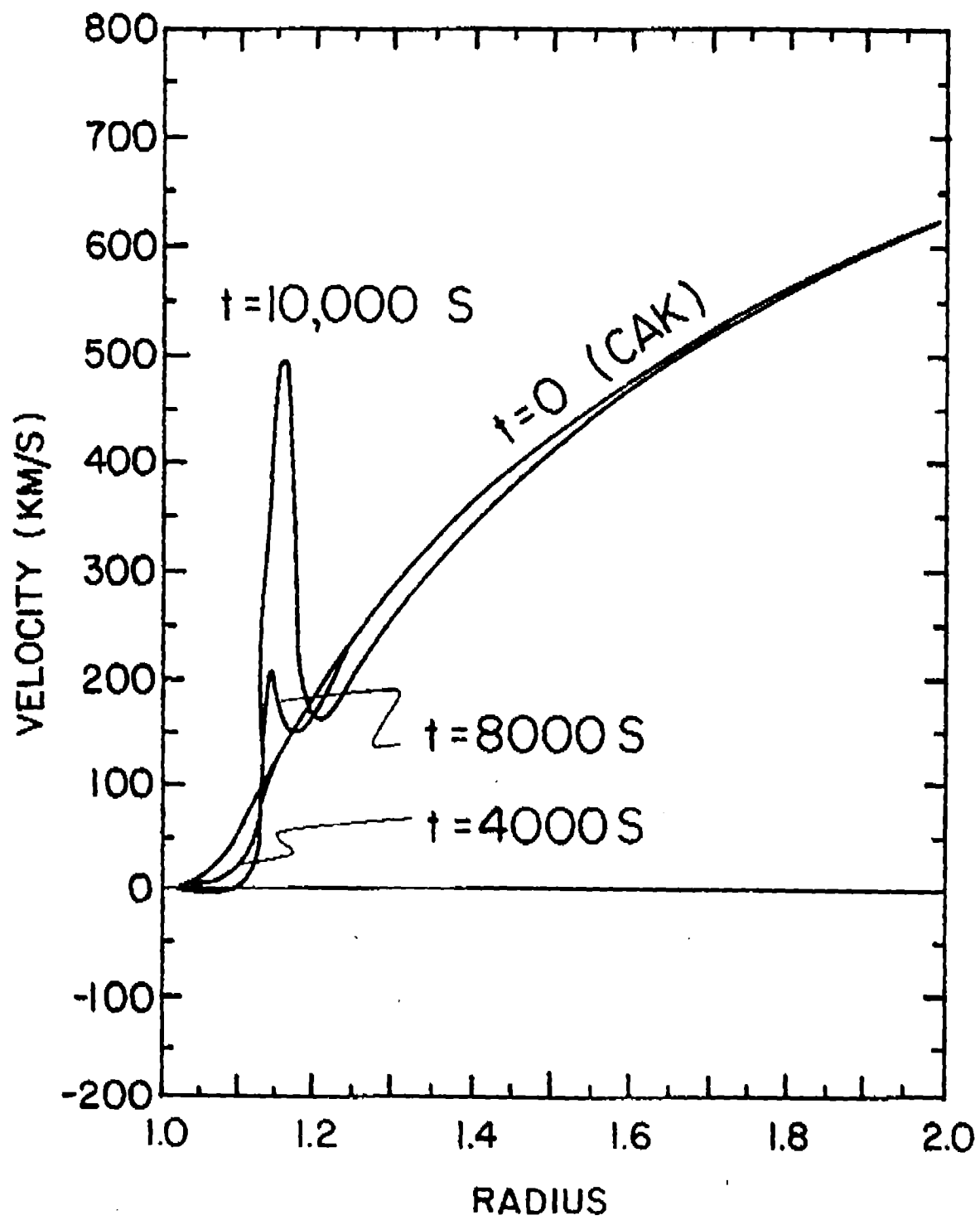


FIGURE 2

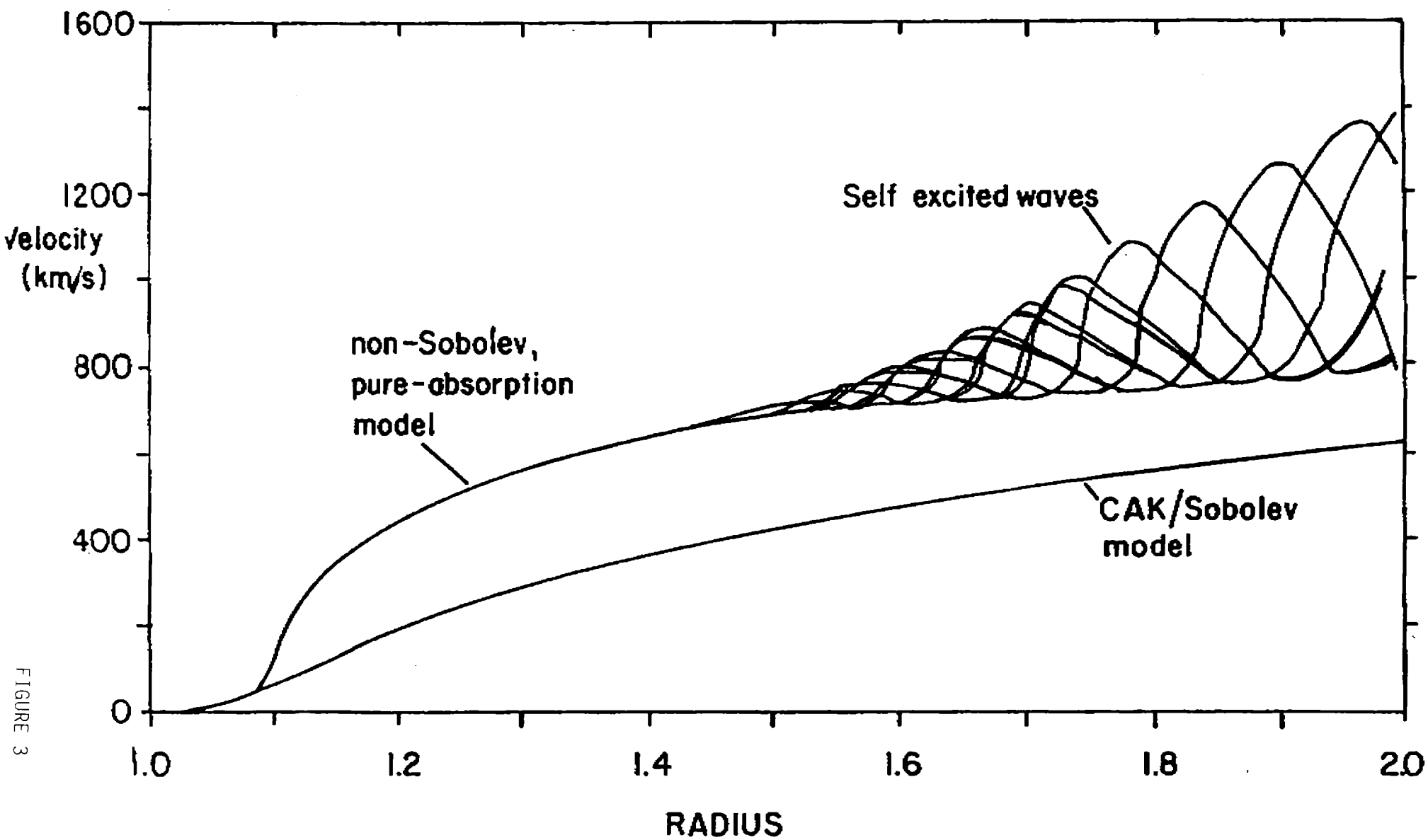


FIGURE 3

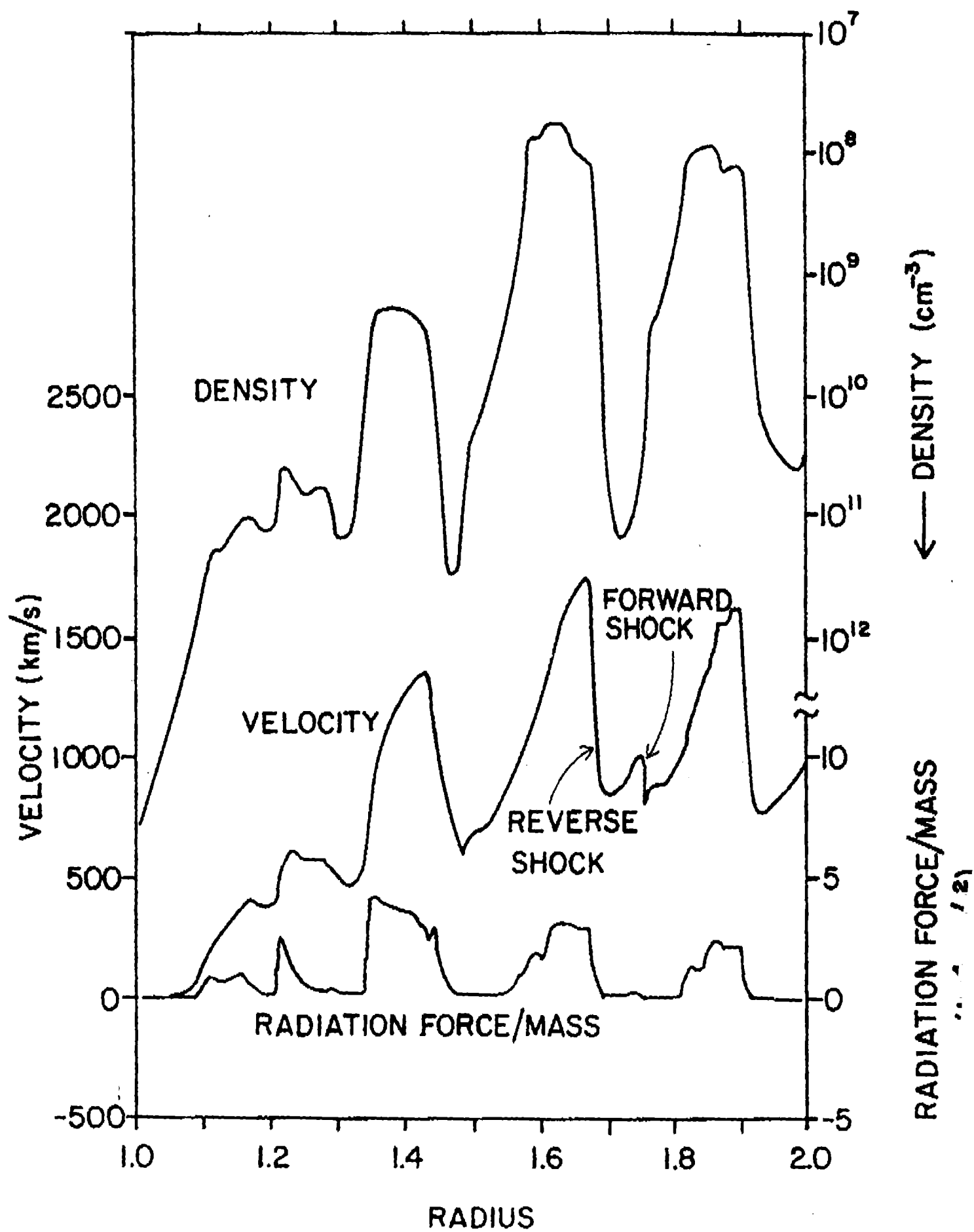


FIGURE 4

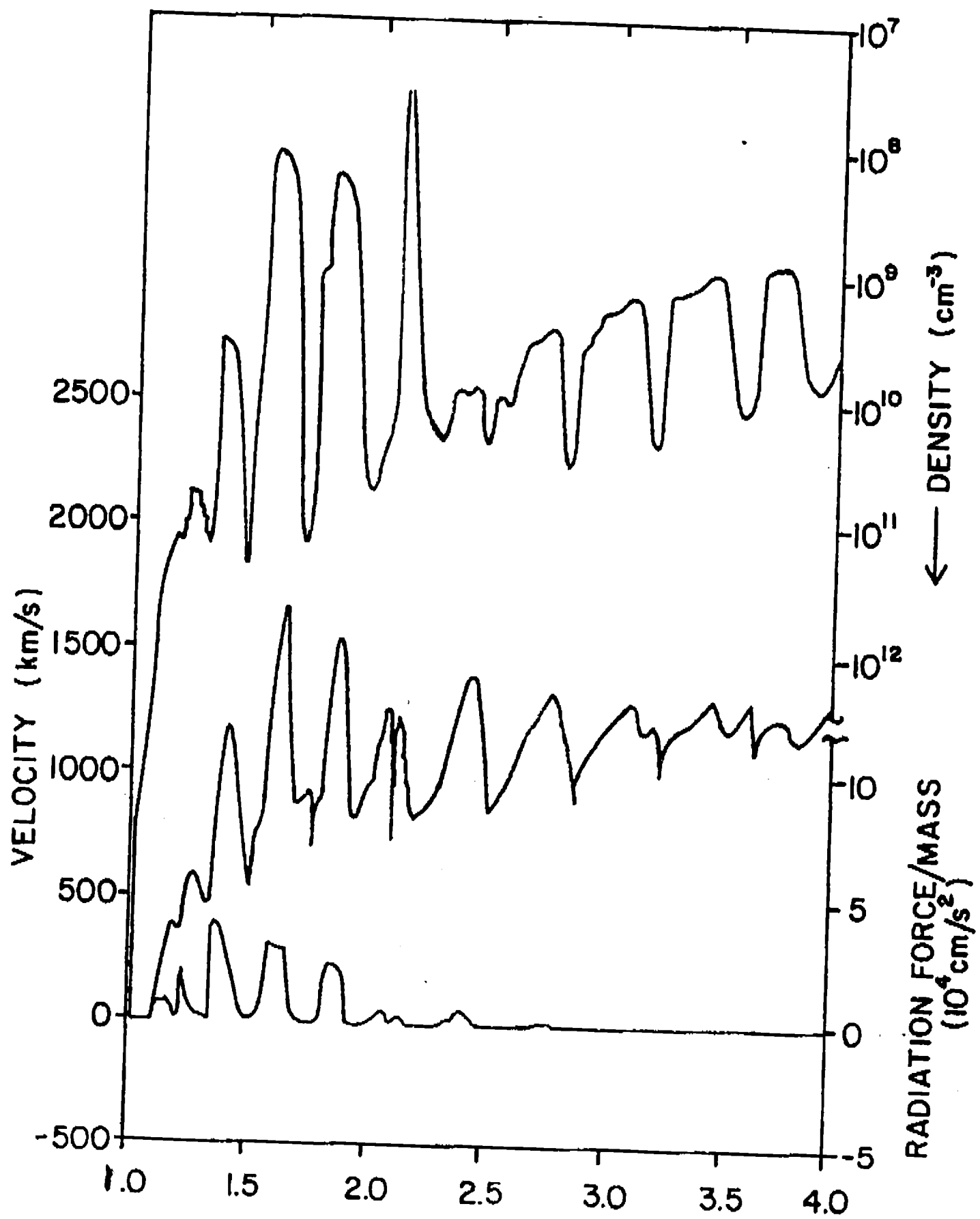


FIGURE 5

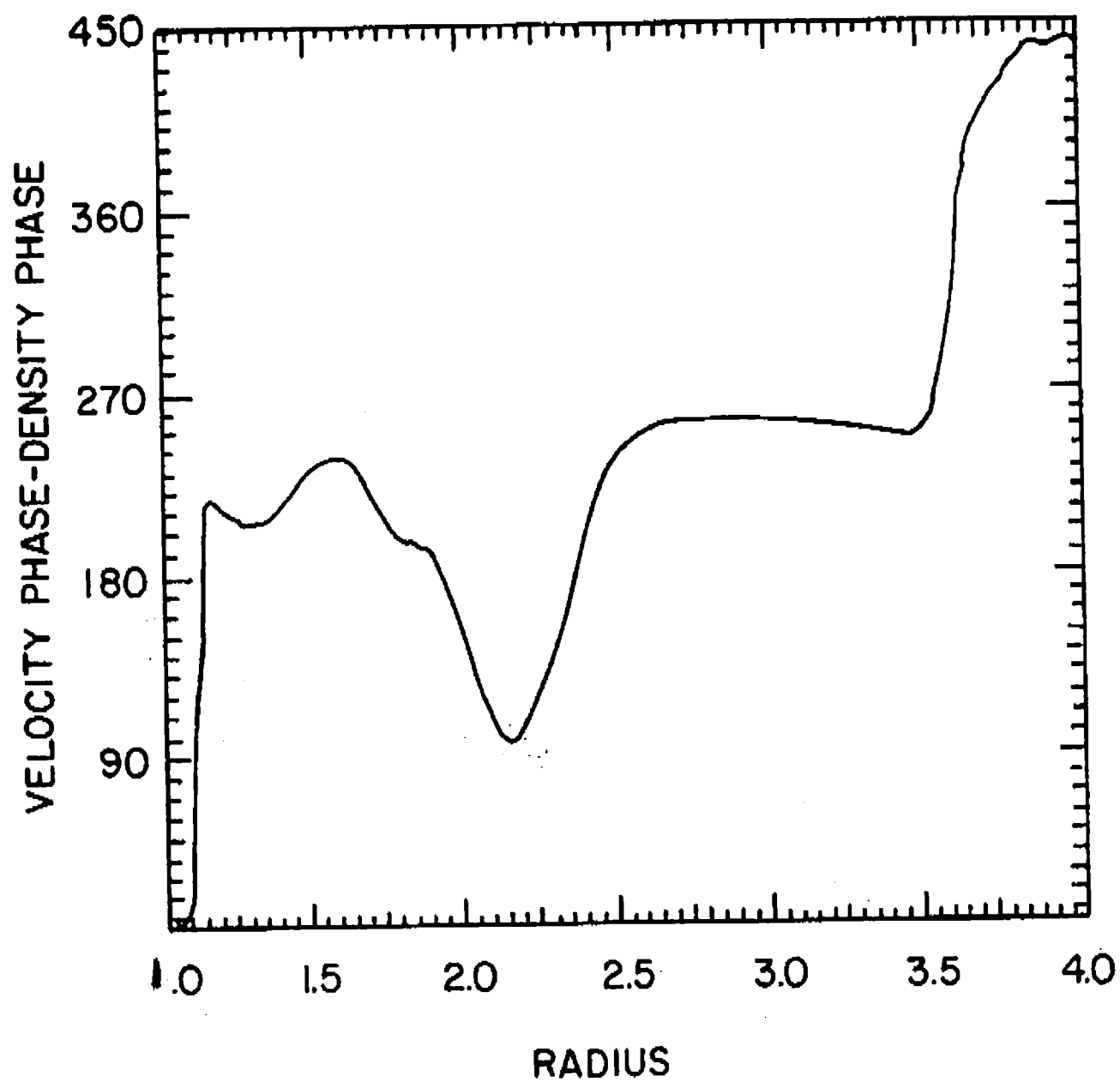


FIGURE 6

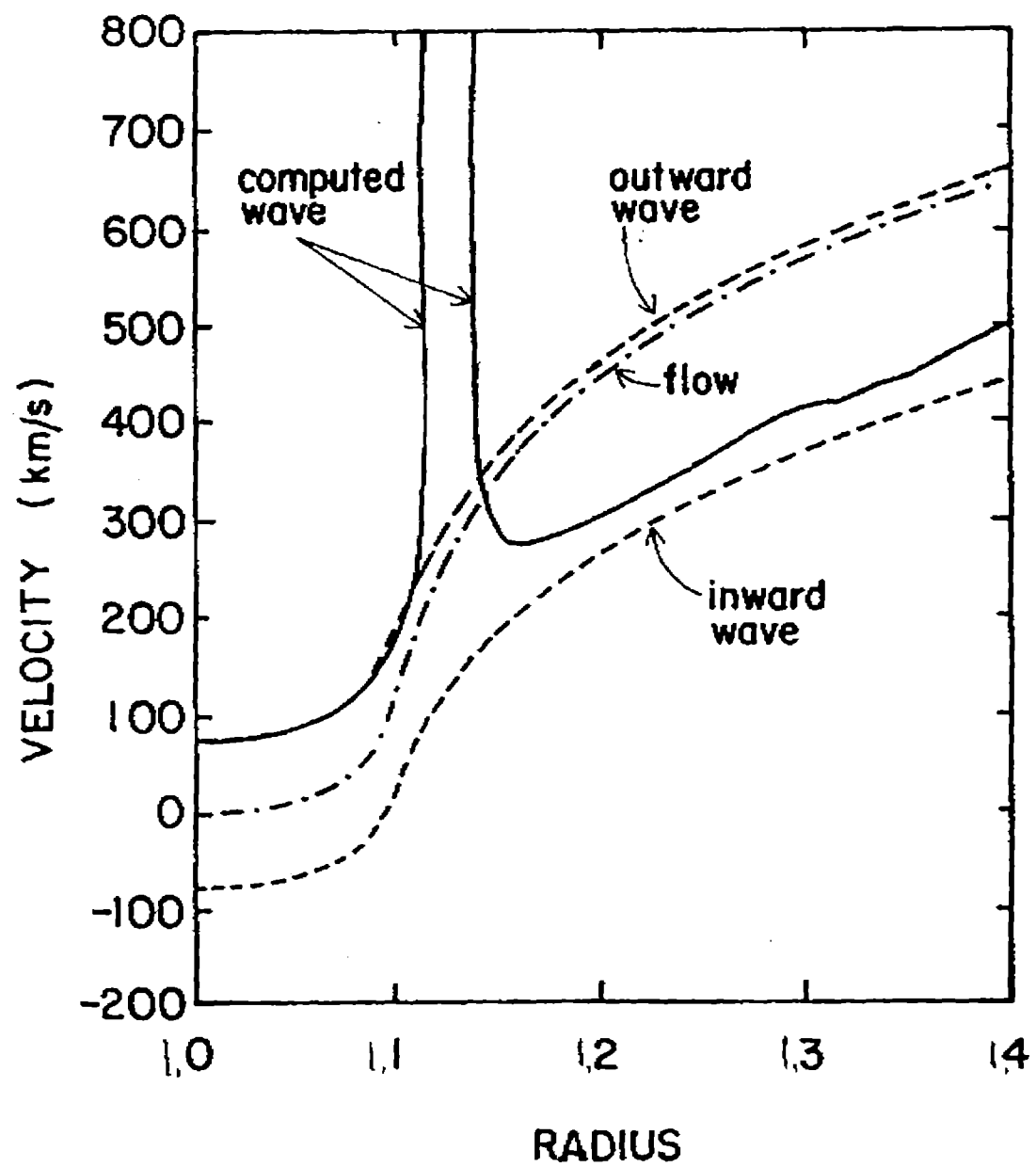


FIGURE 7

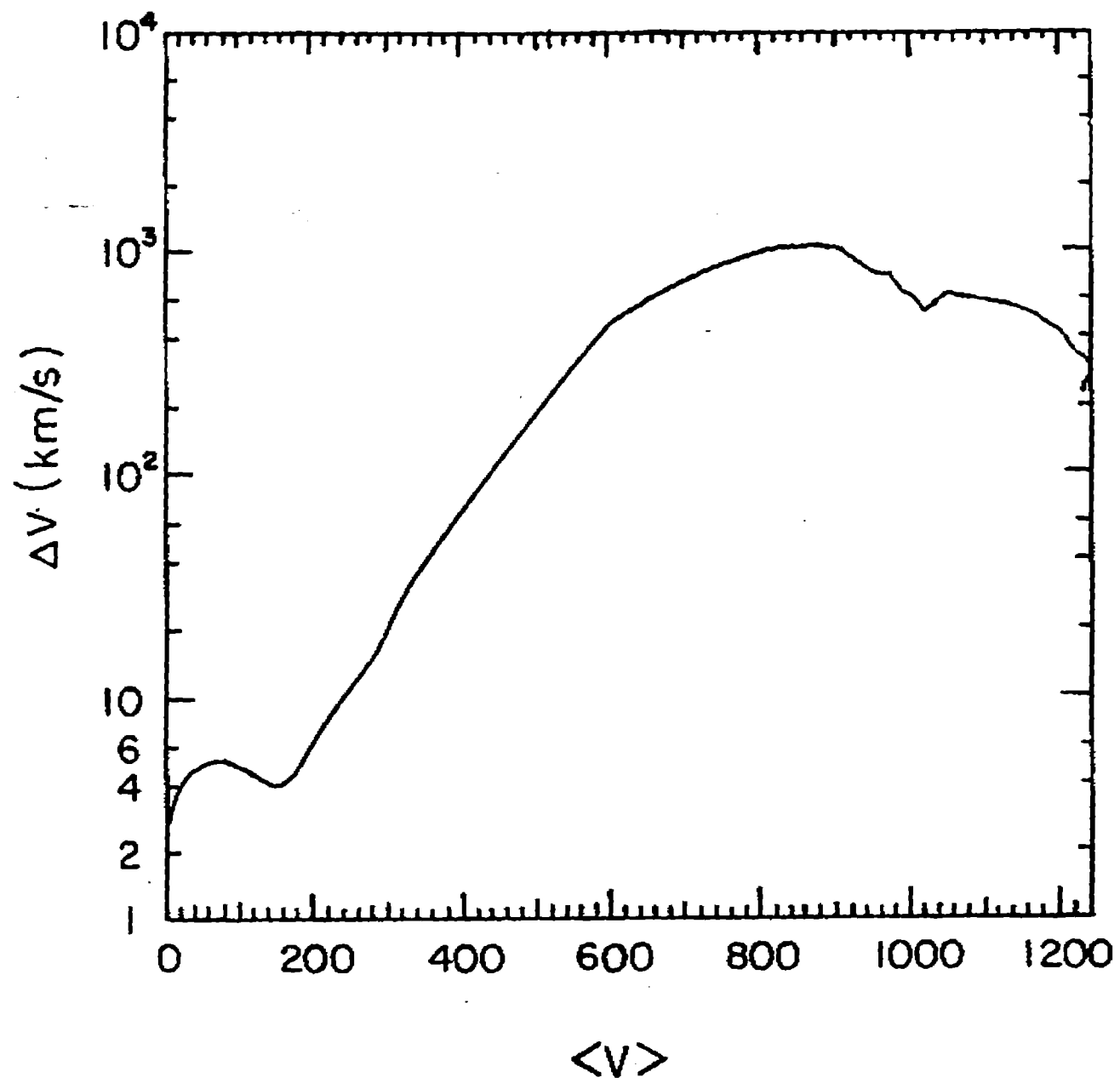


FIGURE 8

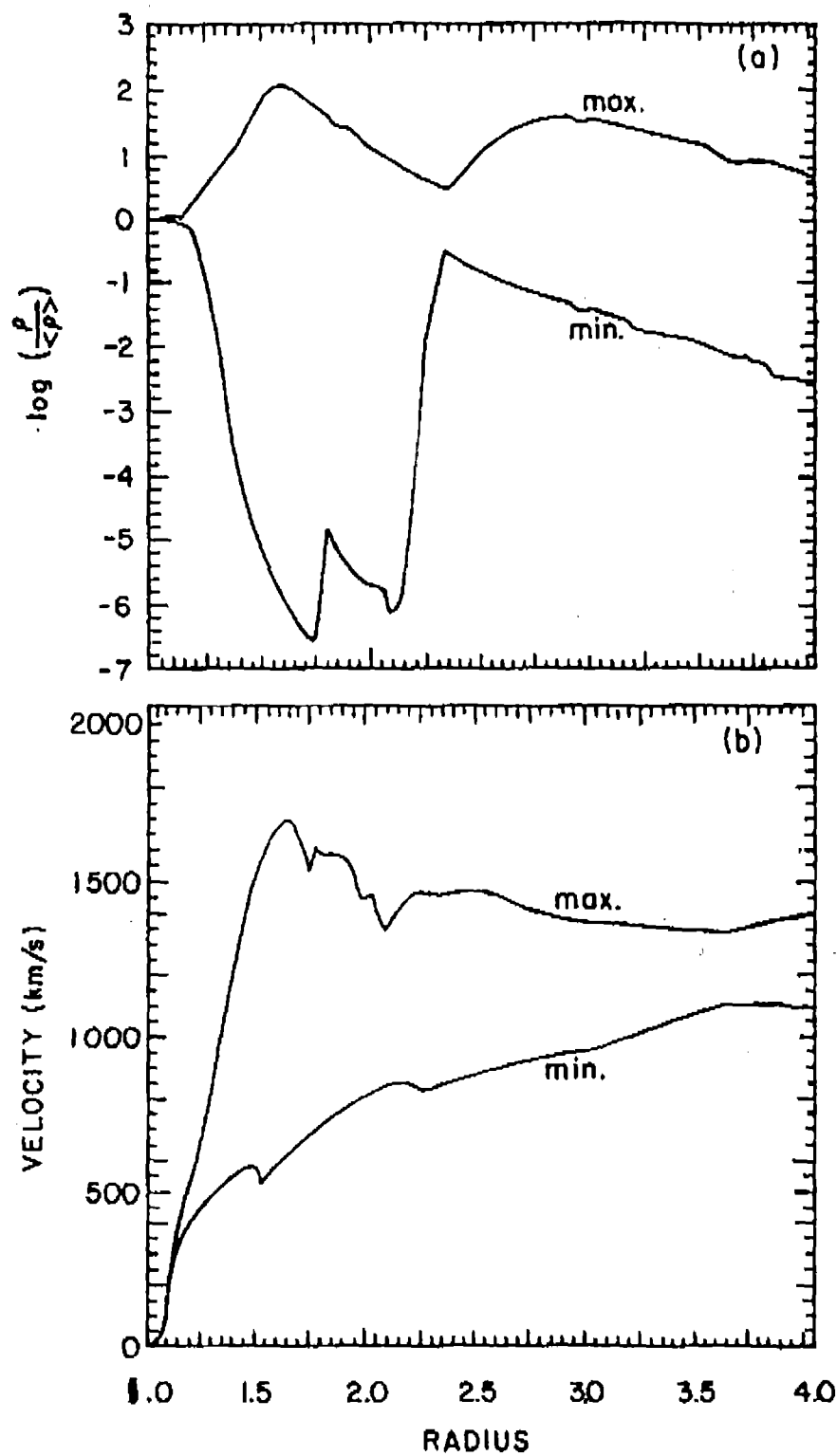


FIGURE 9

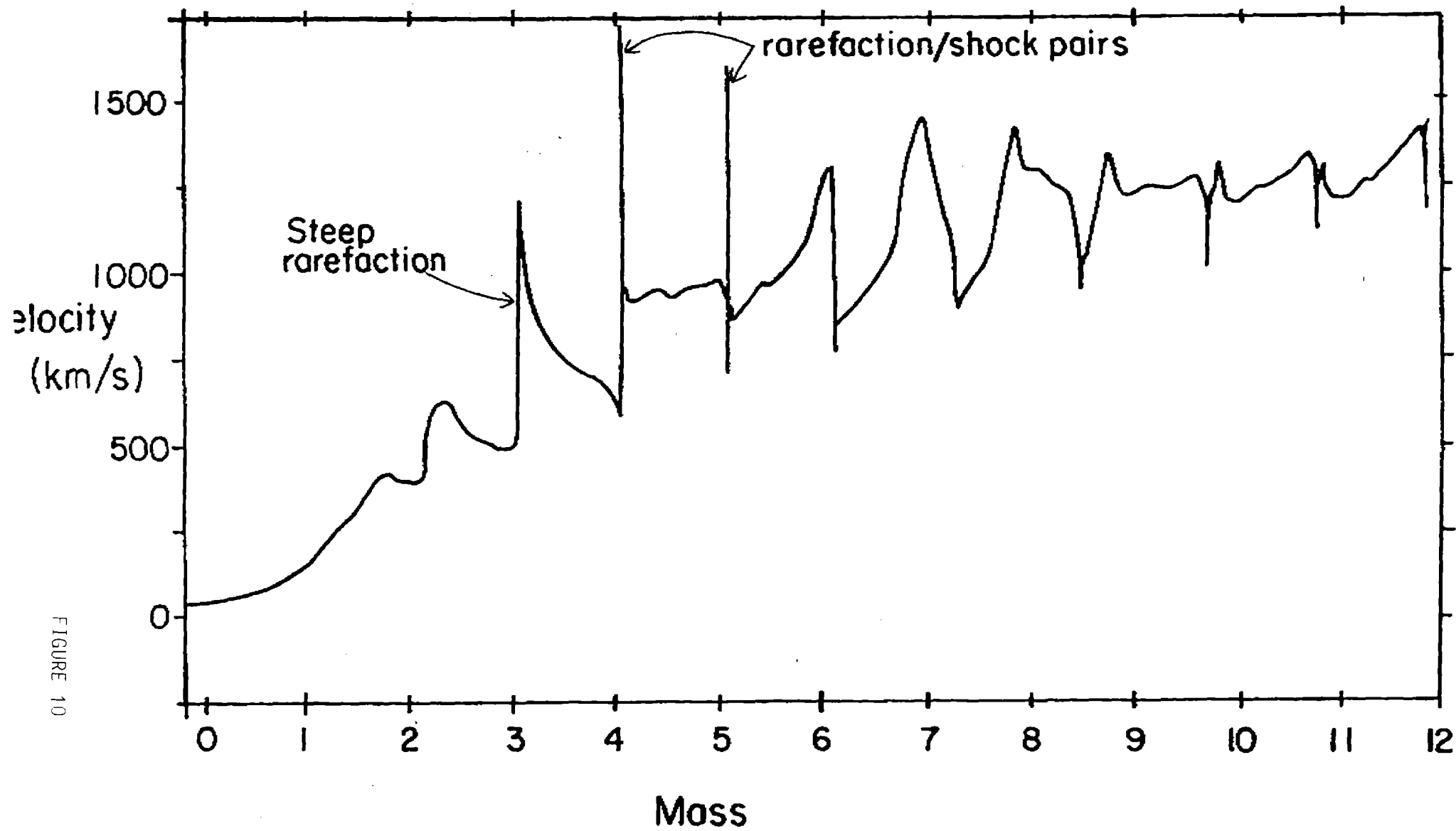


FIGURE 10

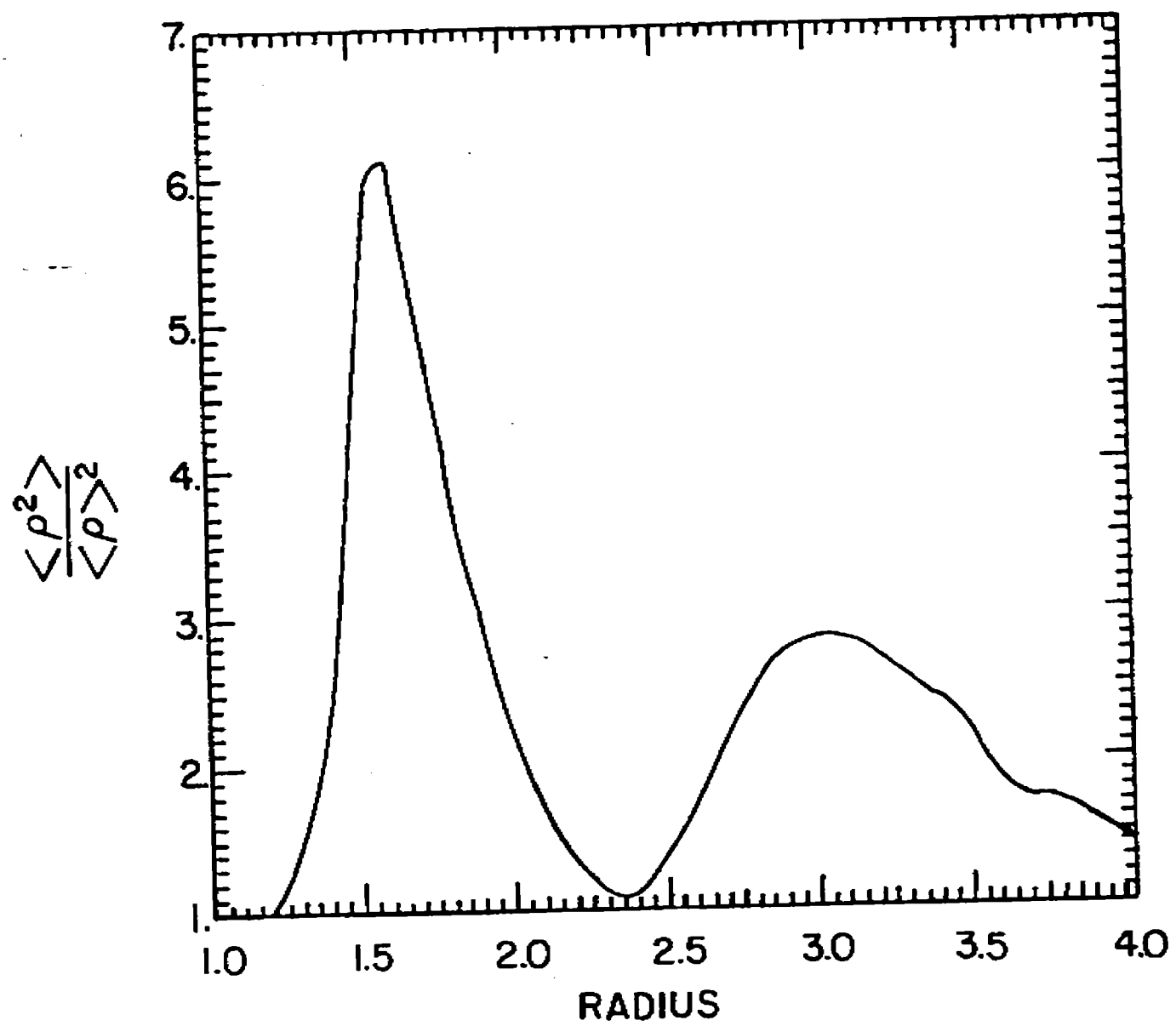


FIGURE 11

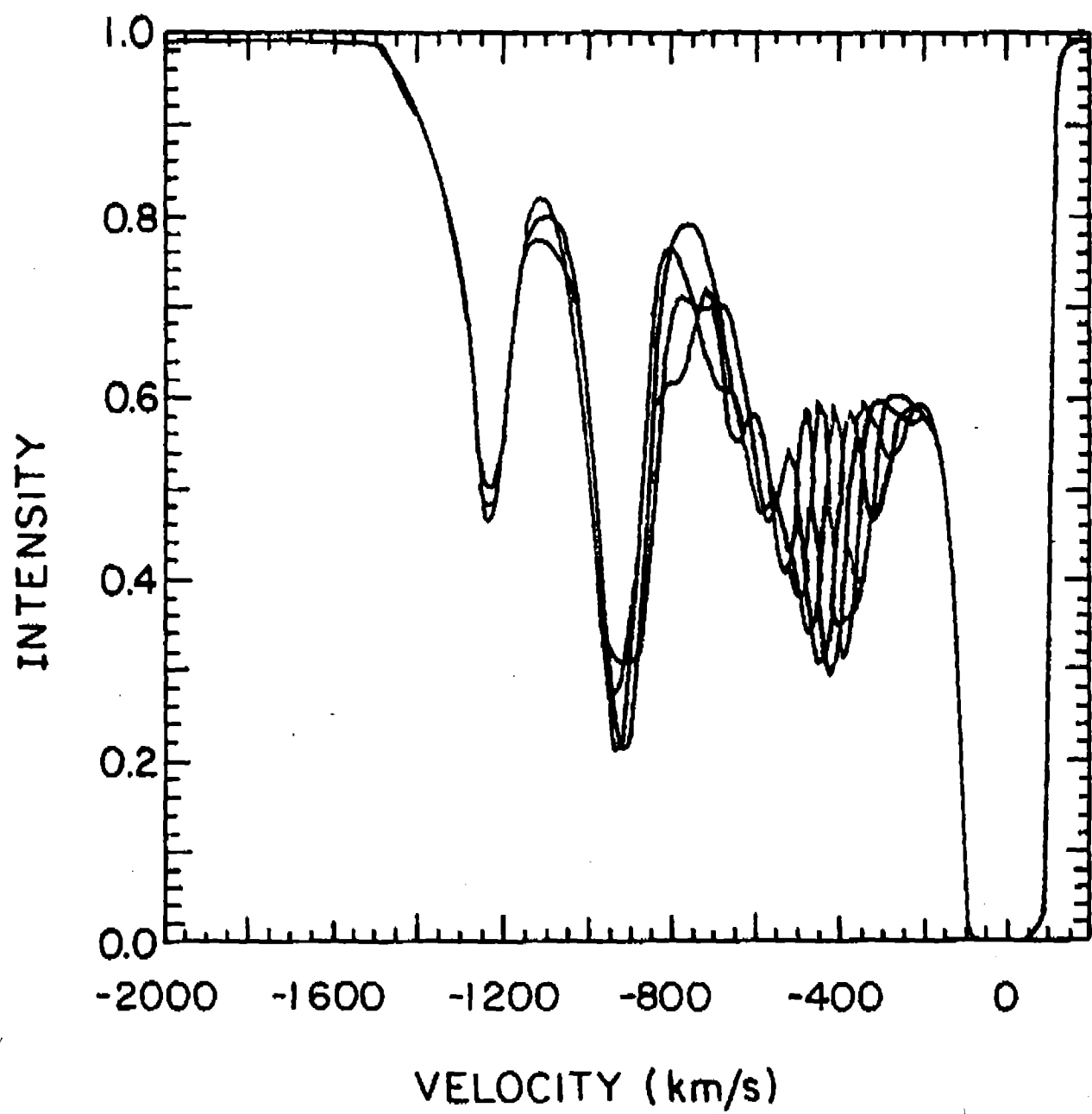


FIGURE 12